Waste and Biomass Valorization
https://doi.org/10.1007/s12649-026-03498-y

ORIGINAL PAPER

Cerium Hexacyanoferrate/NPCQD Hybrid Derived from *Syzygium cumini* Peel for Enhanced Supercapacitor Performance

D. Sivagurunathan[1] · S. Kumaran[2] · K. Umapathy[3] · Simon Deepa[4] · R. A. Kalaivani[1] · P. Siva Karthik[5]

Received: 4 July 2025 / Accepted: 19 January 2026

Abstract

Recent interest in sustainable electrode materials has surged due to the increasing demand for energy storage systems that are both highly efficient and environmentally friendly. In this study, a hybrid electrode composed of cerium hexacyanoferrate (CeHCF) and nitrogen, phosphorus co-doped carbon quantum dots (NPCQDs) derived from *Syzygium cumini* (jamun) peel was synthesized through a simple co-precipitation method. The structure and morphology were comprehensively characterized using XRD, FTIR, SEM, TEM, XPS, and BET analyses. The incorporation of biomass-derived NPCQDs significantly enhanced the conductivity, surface area, and defect density of CeHCF. As a result, the CeHCF/NPCQD electrode exhibited a high specific capacitance of 786 F g^{-1} at 1 A g^{-1} in a three-electrode configuration and retained 91.6% of its initial capacitance after 10,000 cycles. When assembled into an asymmetric CeHCF/NPCQD‖AC device, it delivered a specific capacitance of 248 F g^{-1}, an energy density of 87.8 Wh kg^{-1}, and a power density of 800 W kg^{-1}. The remarkable electrochemical performance arises from the synergistic redox activity of CeHCF and the conductive, defect-rich NPCQDs. The use of low-cost biomass precursors and green synthesis further ensures scalability and environmental sustainability, making CeHCF/NPCQD a promising electrode material for next-generation supercapacitors.

Keywords *Syzygium cumini* derived NPCQD · CeHCF/NPCQD hybrid electrode · ASC device

Introduction

The growing global energy demand, rapid industrialization, and environmental concerns associated with fossil fuel consumption have intensified the need for clean and sustainable energy technologies [1]. Excessive reliance on fossil fuels contributes to ecological degradation, global warming, and greenhouse gas emissions [2]. Therefore, developing efficient energy storage and conversion systems is crucial for supporting renewable sources such as solar and wind, while reducing dependence on non-renewable resources.

Supercapacitors (SCs), also known as electrochemical capacitors (ECs), have attracted significant attention as promising energy storage devices due to their rapid charge–discharge capability, long cycle life, and high-power density compared to batteries [3, 4]. Notwithstanding these advantages, their comparatively low energy density continues to pose a significant difficulty. Consequently, the advancement of high-performance electrode materials is crucial for reducing the performance gap between SCs and batteries. To overcome this issue, hybrid electrode materials that combine the capabilities of several functional components have been extensively studied to enhance the overall electrochemical performance of supercapacitors [5, 6]. Materials such as black phosphorus [7], metal oxides [8], binary/ternary metal compounds [9–11], and Prussian blue analogues (PBAs) [12] have shown great promise when

✉ R. A. Kalaivani
director.sbs@velsuniv.ac.in

1 Centre for Energy and Alternative Fuels, Department of Chemistry, School of Basic Sciences, Vels University, Pallavaram, Chennai, Tamil Nadu 600117, India

2 Department of Electronics and Communication Engineering, Saveetha School of Engineering, Saveetha Institute of Medical and Technical Sciences (SIMATS), Thandalam, Chennai, Tamil Nadu 602105, India

3 Department of Electronics and Communication Engineering College, Rajalakshmi Engineering College, Thandalam, Chennai, Tamil Nadu 602105, India

4 Department of Chemistry, Vels Institute of Science and Technology and Advanced Studies, Pallavaram, Chennai, Tamil Nadu 600117, India

5 Department of Chemistry, University College of Engineering, Panruti, Tamil Nadu 607106, India

Published online: 04 February 2026

combined with carbonaceous substrates, owing to their synergistic pseudocapacitive behavior.

Among these, Metal hexacyanoferrates (MHCFs), a subclass of PBAs, are emerging as a flexible family of materials for energy storage applications due to their distinct structural and electrochemical characteristics [13]. PBA has a unique open three-dimensional double perovskite structure made of alternating low-spin Fe-C_6 and high-spin M-N_6 octahedra connected by cyanide bridges. This structural arrangement has several metal active sites and large interstitial gaps, making it ideal for the reversible insertion and extraction of various guest cations [14]. Recently, various MHCF-based materials such as NiHCF/rGO [15], CoHCF/carbon nanofibers [16], Ni-CoFe-PBA/CNTs [17] and MnHCF/PANI/C [18] have been reported to exhibit enhanced capacitance, rate capability, and cycling stability in supercapacitor applications due to their redox-active nature and tunable hybrid structures. Among the various MHCFs explored, cerium hexacyanoferrate (CeHCF) stands out due to the redox flexibility of the cerium ion (Ce^{3+}/Ce^{4+}), which enables multiple electron transfer reactions and enhances charge storage capability [19, 20]. Additionally, the strong metal–ligand bonding and structural robustness of CeHCF contribute to excellent electrochemical stability during repeated cycling. However, similar to other PBAs, CeHCF suffers from low intrinsic electrical conductivity and limited surface area, which restrict ion diffusion and reduce rate performance in practical applications. Therefore, the development of CeHCF-based composite structures with conductive carbonaceous materials has become an effective strategy to unlock its full electrochemical potential in supercapacitor systems.

In order to overcome these constraints, there has been extensive research on the integration of CeHCF with highly conductive and surface-functionalized carbon nanomaterials to optimize electrochemical utilization and improve charge transport [21, 22]. Carbon quantum dots (CQDs) have attracted attention in this context, particularly those doped with heteroatoms such as nitrogen (N) and phosphorus (P), for their exceptional electrical conductivity, large surface area, and capacity to introduce a significant number of defect sites that facilitate the rapid transport of electrons and ions [23]. N, P co-doped carbon quantum dots (NPCQDs) are an ideal candidate for composite electrode materials due to their pseudocapacitive contributions through surface redox reactions [24]. More recently, the biomass-derived CQDs have emerged as a focal point of current research in accordance with sustainable material design and green chemistry concepts. Among many biomass sources, the peel waste of *Syzygium cumini* (Java plum) is a plentiful and underexploited agro-waste, rich in carbon, nitrogenous chemicals, and polyphenols, rendering it an ideal precursor for the synthesis of NPCQDs using a straightforward hydrothermal method [25]. Using such agro-waste provides a cost-effective, sustainable carbon source while reducing environmental burden through value-added transformation.

This study presents a novel hybrid electrode material consisting of CeHCF and NPCQDs obtained from *Syzygium cumini* peel waste. This method utilises the many redox-active sites of CeHCF (Ce^{3+}/Ce^{4+} and Fe^{2+}/Fe^{3+}) while converting agro-waste into functional carbon nanostructures that improve conductivity, surface defect density, and electrolyte accessibility. The incorporation of waste-derived NPCQDs into CeHCF has a dual benefit such as it mitigates the inherent conductivity constraints of PB equivalents and promotes green chemistry and circular economy principles. This represents the first demonstration of a CeHCF/NPCQD hybrid electrode derived from biomass waste, providing a sustainable pathway for high-performance supercapacitors characterized by improved specific capacitance, rate capability, and long-term cycle stability.

Experimental Procedure

Materials

All analytical reagent grade chemicals of cerium (III) chloride heptahydrate ($CeCl_3{\cdot}7H_2O$), potassium hexacyanoferrate (III) (K_3 [Fe $(CN)_6$]), urea, orthophosphoric acid (H_3PO_4), ethanol and potassium hydroxide (KOH), were purchased from Sigma Aldrich Chemicals and Company, Bangalore and they were used as received. Distilled deionized water with a resistivity of 18 MΩ/cm was used to prepare the solutions.

Synthesis of Nitrogen and Phosphorus Co-doped Carbon Quantum Dots (NPCQDs)

The NPCQDs were synthesized from *Syzygium cumini* peel via hydrothermal carbonization route by following the procedure reported earlier [26]. In a typical synthesis, *Syzygium cumini* peels were first collected, properly cleaned using tap water to acquire remove of dust, and then rinsed with deionized water to make NPCQDs. After 3 days of shade drying, the peels were ground into a fine powder. 5 g of the dried peel powder were dissolved in 100 mL of deionized water for the hydrothermal carbonization process. After this, 1 mL of H_3PO_4 (as the phosphorus source) and 2 g of urea (as the nitrogen source) were added. To ensure thorough mixing, the mixture was stirred for 30 min. The resultant suspension was placed in a 150 mL Teflon-lined autoclave and subjected to heating at 200 °C for 8 h. Upon the autoclave's natural cooling to ambient temperature, a dark brown solution was acquired. The solution performed centrifugation at 8000 rpm for 15 min to eliminate any unreacted carbon particles. The transparent supernatant was collected and passed through

a 0.22 µm membrane filter to remove fine contaminants. To remove small molecular by-products, the filtered solution was dialyzed using a 1000 Da dialysis membrane for 24 h, with the external water replaced every 4 h. The purified solution was then freeze-dried to obtain NPCQDs as a fine brownish powder.

Synthesis of CeHCF and CeHCF/NPCQDs

CeHCF was synthesized by a co-precipitation technique [27]. First, 0.1 M cerium chloride solution was prepared by dissolving 1.87 g of cerium chloride in 50 mL of deionized water. In a separate beaker, 0.1 M K_3 [Fe $(CN)_6$] solution was prepared by dissolving 1.65 g of K_3 [Fe $(CN)_6$] in 50 mL of deionized water. The 50 mL $CeCl_3$ solution was maintained at room temperature with magnetic stirring at 600 rpm. To prevent cerium hydroxide from forming, 0.1 M HCl was used to reduce the pH of this solution around to about 3. The K_3 [Fe $(CN)_6$] solution was subsequently added carefully, dropwise, at a rate of approximately 1 mL per min with constant stirring. The formation of CeHCF was indicated by the appearance of a light green precipitate as the addition proceeded. The mixture was agitated at room temperature for 4 h after the complete addition of all 50 mL to ensure that the reaction was complete. The precipitate was separated using centrifugation at 8000 rpm for 10 min, thereafter washed thrice with 20 mL of ethanol–water (1:1), and then rinsed with deionized water until the wash water's pH approximated 7. The cleaned product was dried overnight at 60 °C to yield CeHCF powder. After that, the hybrid composite was produced by mixing 50 mL of NPCQD solution with 100 mg of CeHCF powder. To ensure adequate dispersion and particle interaction, the mixture was sonicated for an h at 40 kHz using a bath sonicator. To allow the NPCQDs to anchor on the CeHCF surface, the mixture was magnetically agitated at 600 rpm for 6 h at room temperature subsequent sonication. The composite was subsequently collected by centrifugation at 8000 rpm for 10 min, rinsed twice with 20 mL deionized water to remove free NPCQDs, and dried in an oven at 60 °C for 12 h. In order to fabricate electrodes, the final product was designated as CeHCF/NPCQD.

Fabrication of CeHCF/NPCQD Composite Electrode

The working electrode was constructed using the synthesized CeHCF/NPCQD hybrid material. We prepared a homogeneous slurry by combining 80 wt.% CeHCF/NPCQD, 10 wt.% Super P conductive carbon, and 10 wt.% PVDF binder. At first, a few droplets of NMP were introduced until a uniform and viscous paste was achieved. The slurry was subsequently applied to a pre-cleaned nickel foam (1×1 cm^2) using a doctor-blade technique. The coated electrodes were vacuum-dried at 80 °C for 12 h, and subsequently subjected to light compression to enhance surface contact and adhesion. The film thickness was determined to be approximately 90 ± 10 µm, and the active material mass deposition on the Ni foam was maintained at approximately 1.3 mg cm^{-2}. For the three-electrode configuration, the CeHCF/NPCQD-coated Ni foam served as the working electrode, Ag/AgCl as the reference electrode, and a platinum wire as the counter electrode. The electrochemical measurements were carried out in 1 M KOH aqueous electrolyte. To construct the asymmetric supercapacitor (ASC), CeHCF/NPCQD-coated Ni foam was used as the positive electrode and commercially obtained activated carbon (AC) coated Ni foam was used as the negative electrode. The mass of each electrode was adjusted based on the charge-balance relation:

$$\text{ChargebalanceforASC massmatching} : m_+C_+V_+ = m\_C\_V\_$$

resulting in an optimized mass ratio of CeHCF/NPCQD: AC ≈ 1: 2. A Whatman glass fibre membrane soaked in 1 M KOH acted as the separator. The device was assembled in a sandwich-type configuration and gently pressed to ensure reliable interfacial contact and reduced contact resistance. The assembled ASC was evaluated under identical testing conditions as the three-electrode system.

Characterization

The phase structure of the synthesized materials was analyzed using X-ray diffraction (XRD) with a PANalytical X'Pert PRO diffractometer fitted with Cu Kα radiation ($\lambda = 1.5406$ Å). Fourier-transform infrared spectroscopy (FTIR) was employed to identify functional groups in the 400–4000 cm^{-1} range using a PerkinElmer Spectrum spectrometer. Transmission electron microscopy (TEM) (JEOL JEM-2100 operated at 200 kV) and scanning electron microscopy (SEM) (ZEISS EVO18) were used to evaluate particle distribution and surface morphology. Using a Micromeritics ASAP 2020 system, the surface area and porosity were determined by Brunauer–Emmett–Teller (BET) analysis. The elemental composition and chemical states were ascertained by X-ray photoelectron spectroscopy (XPS) employing a Thermo Scientific K-Alpha instrument utilizing Al Kα radiation. Electrochemical assessments, comprising cyclic voltammetry (CV), galvanostatic charge–discharge (GCD), and electrochemical impedance spectroscopy (EIS), were conducted utilizing a CHI660E electrochemical workstation. All electrochemical metrics were computed using standard relations as detailed below. For three-electrode tests, mass m refers to the active mass on the working electrode. For two-electrode ASC, m_{tot} is the sum of the active masses on both electrodes.

$$\text{CVbasedspecificcapacitance}, C_{sp} = \frac{\int I(V)dV}{mv\Delta V}$$

$$\text{GCDbasedspecificcapacitance}, C_{sp} = \frac{I\Delta t}{m\Delta V}$$

$$\text{ASC device capacitance}, C_{\text{device}} = \frac{I\Delta t}{m_{\text{tot}}\Delta V}$$

where, I is the discharge current, Δt is the discharge time, ΔV the effective voltage window after removing the instantaneous iR drop and $m_{total} = m_+ + m_-$ The energy and power densities are calculated by using the following equations:

$$E = \frac{1}{2}C_{\text{device}}(\Delta V)^2/3.6$$

$$P = \frac{3600E}{\Delta t}$$

$$\text{Coulombicefficiency}, \eta = \frac{t_{\text{discharge}}}{t_{\text{charge}}} \times 100\%$$

Results and Discussion

Powder XRD Analysis

The crystalline structure and phase purity of NPCQDs, CeHCF, and the CeHCF/NPCQD composite were examined using X-ray diffraction, with the resultant patterns illustrated in Fig. 1. The XRD pattern NPCQDs displays a large diffraction peak centred at 24°, indicative of the (002) plane of graphitic carbon [28]. This extensive peak is indicative of amorphous or weakly crystalline carbon materials and corroborates the existence of graphitic domains in the synthesized NPCQDs. The highly crystalline nature of pristine CeHCF is demonstrated by the sharp and well-defined diffraction peaks at 16.4°, 24.3°, 28.5°, 29.2°, 33.9°, 37.8°, 45.1°, and 57.2° in the XRD pattern. Among these, the peaks at 16.4°, 24.3°, and 29.2° are the most intense, as they correspond to the typical reflections of the face-centered cubic structure of metal hexacyanoferrates [29]. The successful formation of the CeHCF framework through the co-precipitation process is confirmed by these observations. The CeHCF/NPCQD composite exhibits a diffraction pattern that combines characteristics from both components. Significant peaks in the composite can be seen at 14.9°, 16.8°, 18.9°, 24.1°, 26.8°, 29.6°, 34.0°, 38.2°, 45.1°, and 57.2°, which show that the CeHCF crystalline structure was retained during composite synthesis. It is noteworthy that the wide (002) characteristic of graphitic carbon at around 24° is also

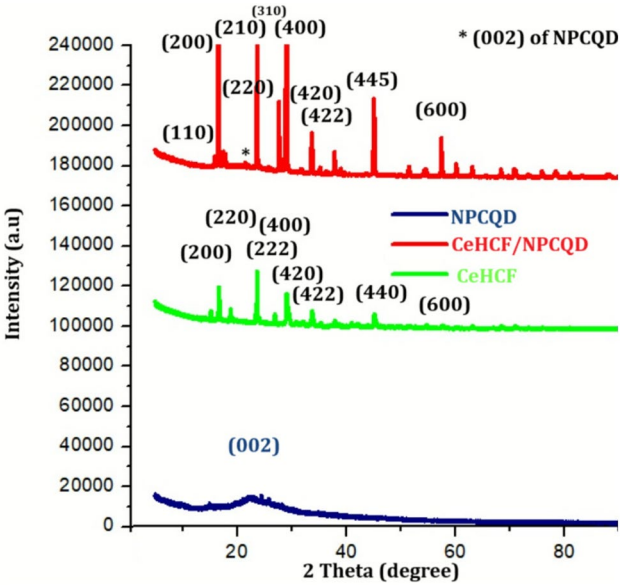

Fig. 1 XRD analysis results of NPCQDs, CeHCF, and CeHCF/NPCQD

visible, indicating that NPCQDs were successfully incorporated into the CeHCF matrix [30]. It's important to note that the diffraction peak strength at 57.2° is much weaker in the mixture than it is in pure CeHCF. This decrease shows that CeHCF and NPCQDs are strongly interacting, which could cause some long-range order to be disrupted or distorted in CeHCF crystallites by changing their surfaces and coming into close touch with the amorphous carbon matrix. Also, small changes and widening of the peaks in the composite help the hybrid form to form successfully, spreading the CeHCF particles out more on the conductive NPCQD network. The XRD results confirm that the CeHCF/NPCQD composite was successfully formed, maintaining the structural integrity of CeHCF while adding NPCQDs to increase overall structural heterogeneity that is advantageous for electrochemical applications because it has more defect sites and better electron transport pathways. (Fig. 2).

FTIR Analysis

The surface functional groups and bonding characteristics of the synthesized NPCQDs were determined using FTIR spectroscopy. The stretching vibrations of O–H and/or N–H groups were ascribed to the broad absorption band in the 3420–3200 cm^{-1} [31]. The stretching vibration of the nitrile (C≡N) groups is responsible for the strong absorption band at 2190 cm^{-1} in the FTIR spectra of NPCQDs. Improved surface reactivity and pseudocapacitive behaviour are caused by these surface functionalities, which are produced during hydrothermal synthesis utilising precursors that are rich in nitrogen. The minor absorption peak at 2162 cm^{-1} is likely

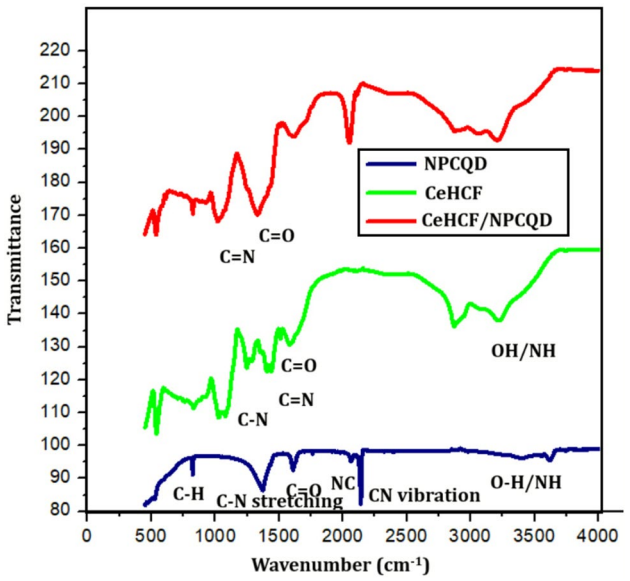

Fig. 2 FTIR spectra analysis results of NPCQDs, CeHCF, and CeHCF/NPCQD

due to weakly conjugated or structurally varied C≡N groups, or possibly isocyanide-like moieties that were formed during hydrothermal synthesis. These variations are indicative of the NPCQDs' chemical heterogeneity and their extensive surface chemistry. The peak at approximately 1620 cm^{-1} is attributed to the C=O stretching of carboxylic groups or the stretching vibration of C=C bonds in the sp^2-hybridized carbon framework [30]. The successful nitrogen doping is confirmed by the characteristic band at 1380 cm^{-1}, which is associated with the C–N stretching vibration of aromatic amines. Additionally, a prominent band observed in the 1230–1180 cm^{-1} range is indicative of the effective incorporation of phosphorus, as it corresponds to the P=O or P–O–C stretching vibrations [32]. The peak at approximately 1080 cm^{-1} is indicative of the presence of oxygenated functional groups, as it can be attributed to the C–O–C or C–OH stretching vibrations. The effective doping of N and P atoms into the carbon framework is confirmed by the abundance of surface functionalities, which substantially contribute to the improved electrochemical activity of NPCQDs. The FTIR spectrum of CeHCF showed a number of prominent peaks in addition to the distinctive metal–cyanide vibrations, which further validate the material's surface chemistry and structural integrity. The in-plane bending vibrations of hydroxyl groups (δO–H) are responsible for the absorption band at 1355 cm^{-1}, which most likely originates from interstitial or lattice-bound water molecules. In somewhat distorted coordination conditions inside the metal–cyanide network, it could also represent small contributions from C–N stretching vibrations. The skeleton vibrations of the Ce–N–Fe bridge, a crucial structural element of the hexacyanoferrate framework, are represented by a clear band seen at 1472 cm^{-1} [33]. The C=N bond vibrations that result from the interaction of cyanide ligands with the cerium centres may potentially contribute to this band. The existence of firmly bonded lattice water inside the structure is further indicated by the peak at 1695 cm^{-1}, which is attributed to the stretching vibrations of carbonyl (C=O) groups or, more likely, to the bending mode of coordinated water (δH–O–H) [34]. The existence of surface functions that might boost electrochemical activity through better wettability and ion transport is confirmed by these extra bands, which also support the CeHCF material's hydrated and structurally coordinated nature. The coordination of metal ions within the hexacyanoferrate lattice is indicated by the peak at 515 cm^{-1}, which is attributed to metal–oxygen (Ce–O and Fe–O) bending vibrations [34]. The out-of-plane deformation of Fe–C≡N groups, which is a common characteristic of Prussian blue analogues, is represented by the 780 cm^{-1} band. In the meantime, the peak at 1065 cm^{-1} is ascribed to C–N stretching vibrations within the cyanide bridge, which serves as confirmation of the metal–ligand bonding in the CeHCF framework [35]. These results show that the structure of cerium hexacyanoferrate was successfully synthesized, which is in line with PB analogues. The FTIR spectrum of CeHCF/NPCQD has a distinct peak at 2076 cm^{-1}, indicative of the C≡N stretching inside the hexacyanoferrate framework. Peaks at 3430 and 1627 cm^{-1} correspond to O–H stretching and H–O–H bending, signifying surface wetness. The band at 590 cm^{-1} corroborates Fe–C bonding. Bands between 1030 and 1220 cm^{-1} are ascribed to C–N/C–O vibrations from NPCQDs, whereas peaks in the 470–550 cm^{-1} range signify Ce–O and Fe–O vibrations. These findings validate the effective creation of hybrids with robust interfacial interactions.

FESEM Analysis

The surface morphology of the synthesized materials was analyzed by field emission scanning electron microscopy (FESEM), with the findings depicted in Fig. 3a–c. As shown in Fig. 3a, NPCQDs exhibited an amorphous and agglomerated morphology with indistinct particulate features as a result of their ultra-small size and high surface energy, which is consistent with their quasi-spherical nanoscale natures. The CeHCF particles were clearly defined polyhedral crystallites with smooth surfaces that clumped together densely. This shape resembles the usual cubic shape of metal hexacyanoferrates, which means that the co-precipitation synthesis progressed well (Fig. 3b). As shown in Fig. 3c, the CeHCF crystallites were observed to be uniformly decorated with the NPCQD clusters in the CeHCF/NPCQD composite. The intercalation of the nanoparticulate NPCQDs across the CeHCF matrix appeared to enhance the surface roughness

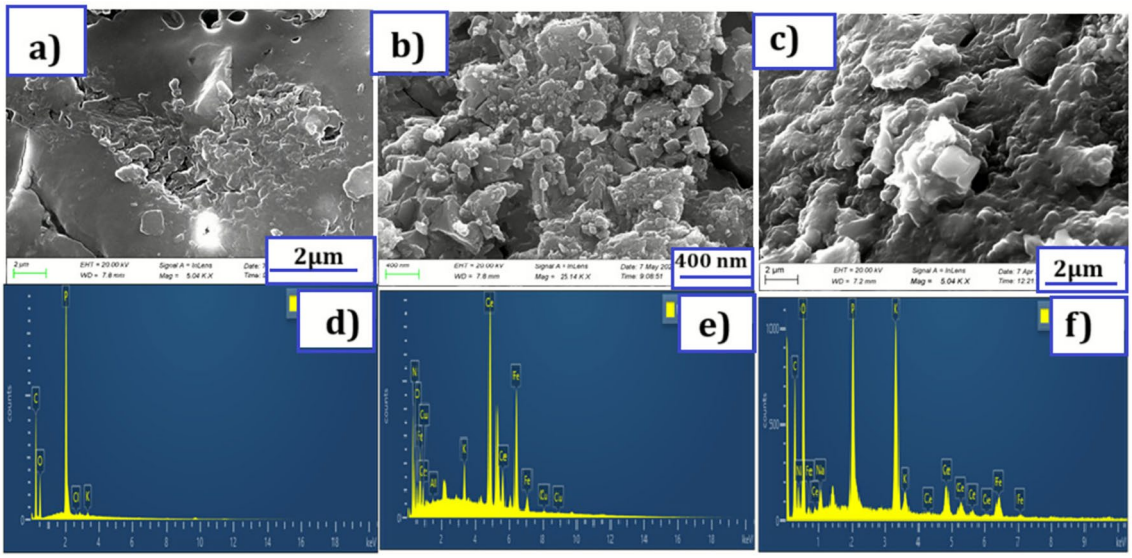

Fig. 3 FESEM images of **(a)** NPCQDs, **(b)** CeHCF and **(c)** CeHCF/NPCQD composite; (d) EDX spectra of CeHCF/NPCQD

and porosity. The corresponding energy-dispersive X-ray (EDX) spectra (Fig. 3d–f) confirmed the elemental composition of all samples. The spectra for NPCQDs revealed prominent signals of C, N, O, and P, verifying the successful N, P co-doping within the carbon framework. CeHCF exhibited distinct peaks corresponding to Ce, Fe, C, and N, consistent with its expected stoichiometry. For the CeHCF/NPCQD hybrid, all these elements (Ce, Fe, C, N, O, and P) were detected simultaneously, confirming the effective integration of NPCQDs within the CeHCF matrix. The EDX elemental mapping (Fig. 4a-c verifies the presence of Ce, Fe, C, N, O, and P in the CeHCF/NPCQD composite, indicating the successful formation of the hybrid material. The NPCQDs are well anchored onto the CeHCF surface, as indicated by the spatially uniform elemental distribution. Nevertheless, it is important to note that the spatial resolution of EDX is significantly greater than the 10 nm size of the NPCQDs. Consequently, EDX offers a bulk-averaged elemental distribution rather than the ability to resolve individual ultrasmall domains. The observed homogeneous mapping, in contrast to an atomically uniform coating, indicates an overall well-integrated hybrid architecture. Therefore, surface-sensitive XPS analysis is employed to further elucidate the subtler details of NPCQD surface localization.

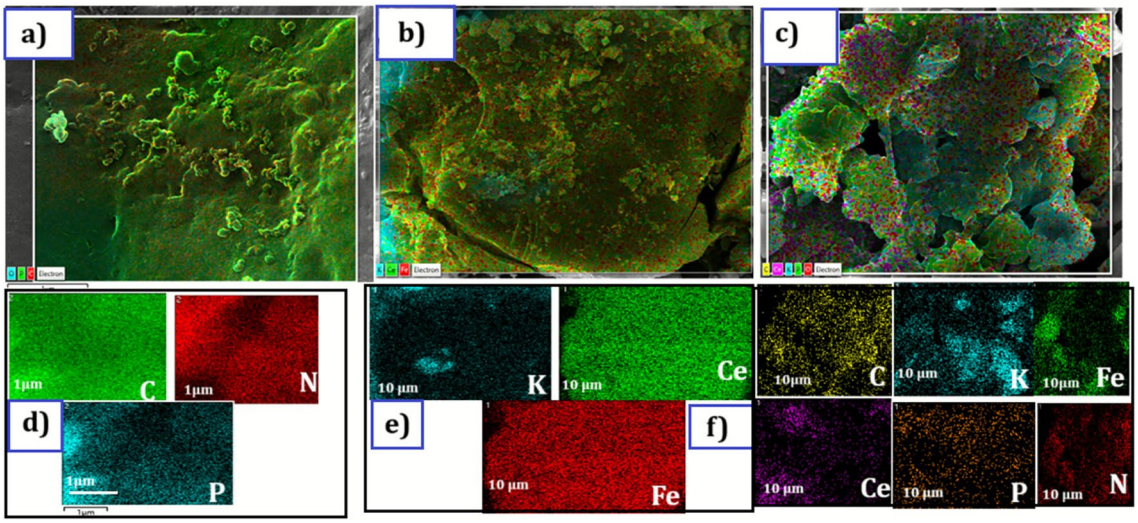

Fig. 4 EDS layered image of **(a)** CeHCF, **(b)** NPCQDs and **(c)** CeHCF/NPCQD composite; **(d–f)** EDS mapping of constituent elements in CeHCF, NPCQD and CeHCF/NPCQD

TEM Analysis

Transmission electron microscopy was utilized to examine detailed molecular features, particle distribution and interfacial structure of the synthesized NPCQDs, CeHCF, and their hybrid composite. Figure 5a illustrates that the NPCQDs possess a quasi-spherical shape with a restricted particle size distribution, primarily less than 10 nm, typical of carbon quantum dots produced during hydrothermal carbonization. The pronounced contrast and uniform distribution indicate limited aggregation and efficient doping of heteroatoms, thereby improving their surface reactivity. Figure 5b displays CeHCF particles with a regular polyhedral shape and sizes ranging from 50 to 100 nm, indicating their crystalline nature. The formation of a face-centered cubic lattice is supported by the uniform morphology and distinct the edges, which are consistent with metal hexacyanoferrate frameworks that have been previously reported. In the hybrid composite image (Fig. 5c), the smaller NPCQDs are evidently adhered to the surface of the larger CeHCF particles. The strong electronic coupling that is necessary to facilitate efficient charge transport pathways and minimize internal resistance during electrochemical operation is suggested by the intimate interfacial contact between the CeHCF crystallites and the NPCQD domains. The crystalline nature of the CeHCF/NPCQD composite is confirmed by HRTEM analysis, which displays distinct lattice fringes with a spacing of 0.366 nm, which corresponds to the (220) plane of CeHCF (Fig. 5d). The existence of NPCQDs is shown by amorphous areas surrounding the particles, which suggests effective hybrid formation with high interfacial contact. The polycrystalline nature of the composite is further confirmed by the SAED pattern (Fig. 5e), which exhibits concentric rings indexed to the (200), (220), (400), and (420) planes of CeHCF. The coexistence of amorphous and crystalline phases is advantageous for the improvement of electrochemical activity and charge transport. Additionally, a statistical particle size analysis was carried out on over 200 individual particles from multiple TEM micrographs in order to quantitatively validate the ultrasmall dimensions of the NPCQDs. The NPCQDs' average diameter of approximately 6–9 nm is confirmed by the particle size histogram, which is consistent with the morphological observations in Fig. 5a. The small size of NPCQDs is particularly advantageous due to its ability to augment the quantity of surface-active sites that perform charge storage and shorten ion diffusion pathways.

Elemental Composition and Chemical Surface State Analysis

XPS analysis was carried out to investigate the surface elemental composition and chemical states of the CeHCF/NPCQD hybrid composite. The composite's successful construction with all anticipated constituent elements is validated by the full scan survey spectrum (Fig. 6a), which confirms the presence of Ce, Fe, C, N, O, and P. The high-resolution Ce 3d spectrum (Fig. 6b) exhibits well-defined spin–orbit doublets at binding energies of approximately 884.6 eV (Ce $3d_{5/2}$) and 907.8 eV (Ce $3d_{3/2}$), which are indicative of the Ce^{3+} oxidation form [36]. The absence of satellite peaks that are typically associated with Ce^{4+} suggests that cerium is primarily in the trivalent state, which is

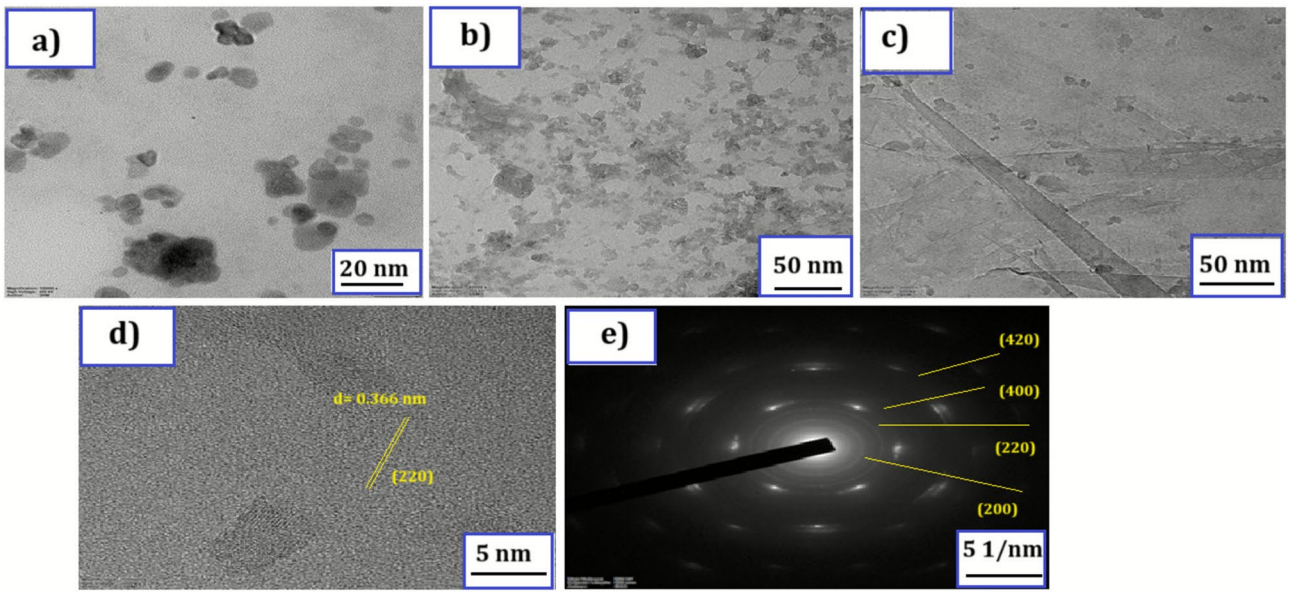

Fig. 5 TEM images of **(a)** NPCQDs, **(b)** CeHCF, **(c)** CeHCF/NPCQD composite; **(d)** HRTEM image of CeHCF/NPCQD **(e)** SAED pattern of CeHCF/NPCQD

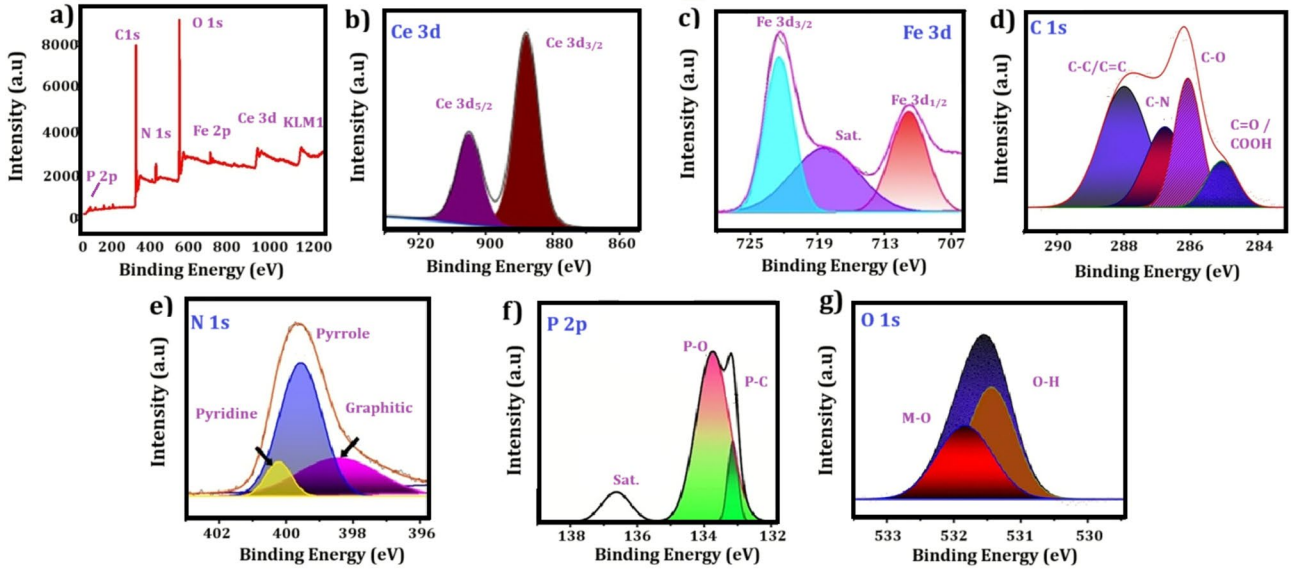

Fig. 6 XPS spectra of CeHCF/NPCQD: **(a)** Full survey, **(b)** Ce 3d, **(c)** Fe 2p, **(d)** C 1 s, **(e)** N 1 s, **(f)** P 2p and **(g)** O 1 s

electrochemically advantageous due to its ability to undergo reversible redox transitions and electron shuttling in charge storage events. The Fe 2p spectrum (Fig. 6c) displays core-level peaks at approximately 710.1 eV (Fe $2p_{3/2}$) and 722.3 eV (Fe $2p_{1/2}$), along with a shake-up satellite at around 717.2 eV, indicating the existence of Fe^{3+} in an octahedral coordination environment, in accordance with the Fe–C≡N bond in the PB structure [37]. This confirms the continuation of the hexacyanoferrate structure after hybridization. The C 1 s spectrum (Fig. 6d) is deconvoluted into several components: a predominant peak at approximately 284.6 eV corresponding to sp^2-hybridized C–C/C=C bonds in graphitic carbon; a shoulder at around 286.2 eV attributed to C–N and C–O functionalities; and a higher binding energy component at approximately 288.4 eV corresponding to carboxyl or carbonyl (C=O) groups [38]. The presence of oxygen- and nitrogen-containing functions signifies surface doping and enhances faradaic pseudocapacitance. The N 1 s spectrum (Fig. 6e) displays three distinctive nitrogen configurations—pyridinic-N (≈398.1 eV), pyrrolic-N (≈399.3 eV), and graphitic-N (≈400.4 eV)—each significantly contributing to the enhancement of the material's electrochemical performance. Pyridinic-N enhances electron donation and the accessibility of active sites, whereas pyrrolic-N promotes reversible redox processes owing to its pentagonal ring configuration [39]. Graphitic-N, incorporated inside the carbon lattice, enhances charge transport by altering electron density. The P–O and P–C bonding environments are identified by the doublet in the P 2p spectrum (Fig. 6f), which is centred at around 133.3 and 134.1 eV, respectively. It is well known that the effective integration of phosphorus into the carbon framework increases conductivity and active surface contacts in electrochemical systems by introducing heteroatom-induced defects and electron-rich sites [40]. The O 1 s core level (Fig. 7(g)) displays two primary peaks: one at approximately 531.1 eV, which is associated with lattice oxygen (M–O, where M=Ce or Fe), and another at approximately 531.7 eV, which is linked to

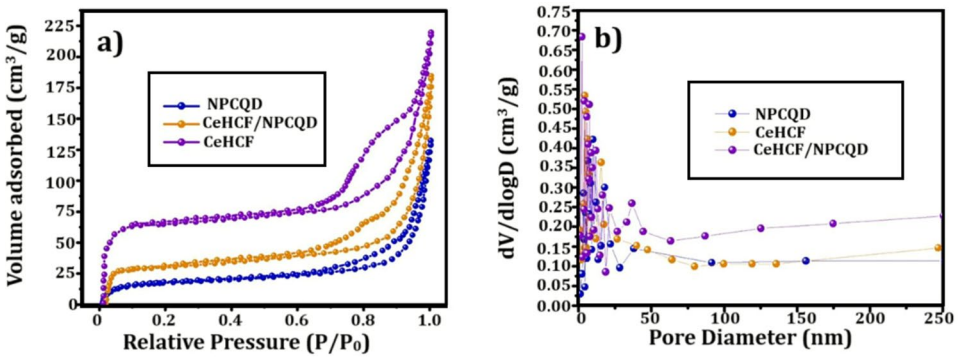

Fig. 7 **(a)** Nitrogen adsorption–desorption isotherms of NPCQDs, CeHCF, and CeHCF/NPCQD composite **(b)** BJH pore size distribution

surface-adsorbed –OH groups and oxygenated species [41]. These oxygen capabilities improve surface wettability and facilitate ion diffusion and electrolyte accessibility The XPS analysis provides additional information about the locations of distribution of NPCQDs in the hybrid architecture when combined with the EDX data. XPS probes only the top few nm of the surface, whereas EDX gives the bulk-averaged elemental composition. Therefore, the CeHCF/NPCQD composite's comparatively greater N 1 s and P 2p signals suggest that the heteroatom-rich carbon domains are primarily found close to the CeHCF crystallite's exterior rather than evenly dispersed throughout their core. This observation is consistent with the TEM images, which display ultrasmall NPCQDs adorning the bigger CeHCF particle's exterior surfaces. This type of surface-anchored structure promotes effective electrolyte penetration, increases the number of electrochemically accessible active sites, and accelerates interfacial charge transfer. All of these elements interact to produce the significant capacitive contribution and decreased charge-transfer resistance expected in the electrochemical studies. The qualitative characterization of chemical states, along with the elemental composition derived from the XPS survey spectra, verified that the NPCQDs comprised roughly 5–7 at. % N and 1–2 at. % P. The deconvolution of the N 1 s spectrum indicated the existence of both pyridinic-N and pyrrolic-N functionalities, which are recognized for creating localized electron-rich sites and augmenting the intrinsic redox activity of the carbon domains. The P 2p spectrum similarly revealed contributions from P–C and P–O bonding environments, indicating the efficient incorporation of phosphorus atoms into the carbon framework rather than their presence as surface residues. The dual heteroatom doping creates extra defect sites, alters electronic charge distribution, and enhances interfacial charge transfer. The aforementioned properties collectively boost conductivity and accelerate electron/ion dynamics in the CeHCF/NPCQD hybrid electrode relative to pure CeHCF.

Textural Analysis

The textural characteristics of NPCQDs, CeHCF, and the CeHCF/NPCQD composite were analysed using nitrogen adsorption–desorption analysis, as depicted in Fig. 7a–b. All samples display Type-IV isotherms associated with H_3-type hysteresis loops, indicative of mesoporous structures composed of aggregated nanocrystalline domains [42]. The BET surface area of pure CeHCF was determined to be 43.2 $m^2\ g^{-1}$, with a total pore volume of 0.18 $cm^3\ g^{-1}$ and an average pore width of around 3.4 nm, indicating the existence of thin interparticle mesopores linked to its polyhedral crystallites. Conversely, the NPCQDs exhibit a markedly elevated surface area of 124.6 $m^2\ g^{-1}$, alongside a pore volume of 0.32 $cm^3\ g^{-1}$ and an average pore width of around 2.8 nm, which aligns with their diminutive particle size and defect-laden carbon framework generated during hydrothermal carbonization. The CeHCF/NPCQD composite exhibits a surface area of 86.7 $m^2\ g^{-1}$, an intermediate pore volume of 0.26 $cm^3\ g^{-1}$, and a widened mesopore distribution centered at around 4.6 nm. The expansion of pore width and slight increase in pore volume relative to pristine CeHCF suggests that the inclusion of NPCQDs inhibits dense crystallite agglomeration, creates interfacial voids, and establishes extra ion-accessible channels [43]. This hierarchical mesoporous network facilitates rapid electrolyte infiltration and minimizes ion-diffusion distances, thus enhancing the usage of redox-active Ce^{3+}/Ce^{4+} and Fe^{2+}/Fe^{3+} sites. The increased accessible surface area and expanded mesoporosity of the CeHCF/NPCQD hybrid directly contribute to its superior capacitance, improved charge–discharge reversibility, and exceptional high-rate performance demonstrated in subsequent electrochemical studies [44, 45]. (Table 1)

Electrochemical Performance of CeHCF and CeHCF/NPCQD in Three Electrode System

CV Analysis

The electrochemical behaviour of CeHCF, and the CeHCF/NPCQD hybrid electrode was investigated using cyclic voltammetry in 1 M KOH (Fig. 8a-b). As shown in Fig. 8a, pristine CeHCF displays clear redox peaks from the Fe^{2+}/Fe^{3+} and Ce^{3+}/Ce^{4+} couples, confirming pseudocapacitance behaviour. However, the peaks are broader with lower currents, reflecting limited ion-accessible sites and low intrinsic conductivity [45]. Conversely, the CeHCF/NPCQD hybrid electrode exhibits a markedly larger enclosed CV area and more pronounced, symmetrical redox peaks across all scan rates (Fig. 8b). This augmentation signifies accelerated electron transport, increased exposure of electroactive sites, and enhanced redox reversibility. The hybrid electrode preserves its cyclic voltammetry profile at elevated sweep rates, indicating superior rate capability and swift ion diffusion. The enhanced responsiveness is due to the conductive N, P-doped carbon quantum dots, which create highly accessible charge-transport channels and inhibit the dense aggregation of CeHCF crystallites [46, 47]. The specific

Table 1 BET surface area, pore volume, and average pore size of NPCQDs, CeHCF, and CeHCF/NPCQD composite

Sample	BET surface area (m^2/g)	Pore volume (cm^3/g)	Pore diameter (nm)
NPCQD	124.6	0.215	2.1
CeHCF	43.2	0.089	2.3
.CeHCF/NPCQD	86.7	0.146	3.5

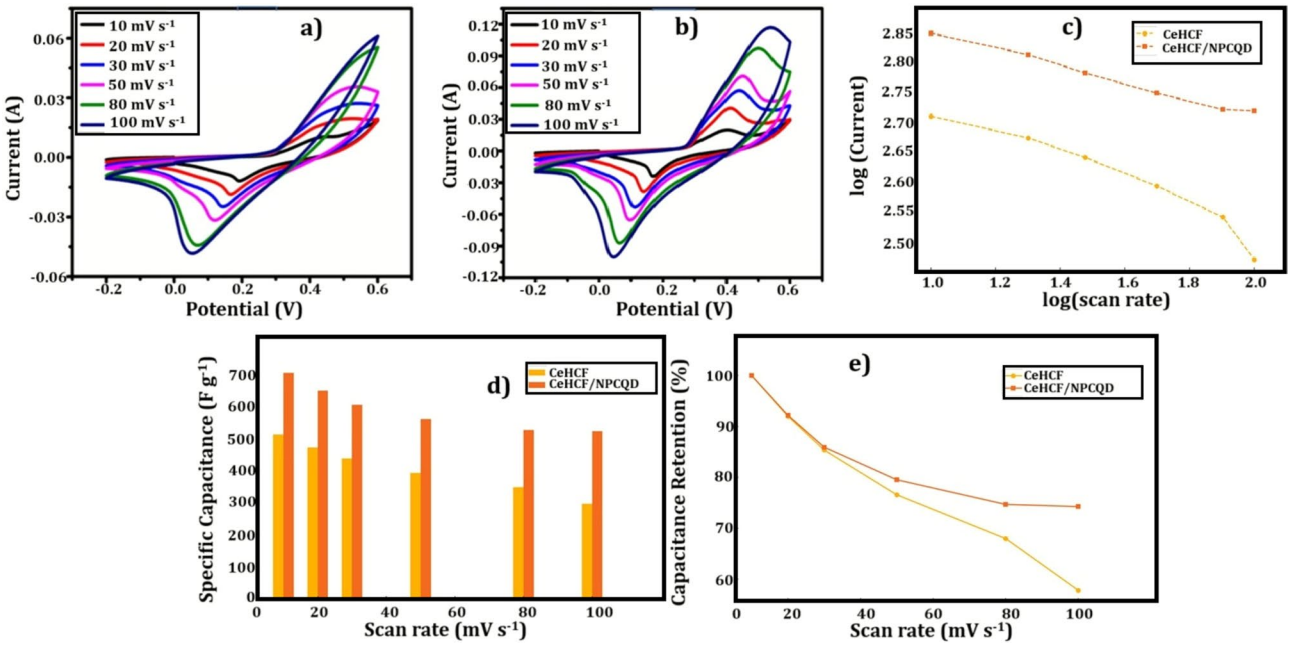

Fig. 8 CV profiles of **(a)** CeHCF and **(b)** CeHCF/NPCQD at different scan rates **(c)** Plot of log(i) vs. log(v) **(d)** Plot of specific capacitance vs. scan rate for CeHCF and CeHCF/NPCQD (e) Capacitance retention Vs scan rate

capacitance calculated from the CV curves confirms this enhancement. At a scan rate of 10 mV s^{-1}, the CeHCF/NPCQD hybrid delivers a specific capacitance of 703 F g^{-1}, outperforming pristine CeHCF (512 F g^{-1}) and NPCQDs (64 F g^{-1}). When the scan rate increases to 100 mV s^{-1}, the hybrid retains ≈ 74% of its initial capacitance, whereas CeHCF maintains only ≈ 58%, highlighting the superior rate capability and stable charge-transfer dynamics of the composite electrode.To gain deeper insight into the charge storage mechanism of the CeHCF/NPCQD hybrid, several electrochemical parameters were derived from CV analysis. The dependence of peak current (i) on scan rate (v) follows the power law relation $i = a \cdot v^b$ [48]. The b-value differentiates between diffusion-controlled (b ≈ 0.5) and surface-controlled (b ≈ 1) processes [49]. The CeHCF/NPCQD electrode shows a b-value of 0.93 (Fig. 8c), indicating that the charge storage process is primarily surface-controlled and pseudocapacitive. In comparison, pristine CeHCF exhibits a lower b-value of 0.74, suggesting a greater diffusion-limited contribution due to fewer electroactive sites and lower conductivity [50]. The reversibility of the redox process was further assessed by evaluating the peak-to-peak separation (ΔE_p). The CeHCF/NPCQD hybrid demonstrates a reduced ΔE_p of 81 mV, in contrast to 127 mV for pristine CeHCF, hence affirming enhanced electron-transfer kinetics and superior reversibility [51]. Dunn's model was utilized to differentiate between capacitive and diffusion-controlled contributions. At a scan rate of 20 mV s^{-1}, the hybrid electrode exhibits a 76% capacitive contribution, markedly above the 51% observed for CeHCF. The elevated capacitive ratio underscores the predominant surface-confined redox mechanism enabled by the hybrid structure. The CeHCF/NPCQD system operates through a synergistic mechanism. CeHCF imparts pseudocapacitance via reversible Ce^{3+}/Ce^{4+} and Fe^{2+}/Fe^{3+} transitions, while the NPCQDs enhance faradaic activity through surface functional groups, including pyridinic-N, pyrrolic-N, graphitic-N, and P–O/P–C bonds. The intimate interfacial contact between CeHCF crystallites and the conductive NPCQD network diminishes charge-transfer resistance, improves electrolyte infiltration, and facilitates rapid, reversible redox reactions at near-surface locations. The specific capacitance (C_s) was calculated from the CV curves by utilizing the integrated area, scan rate, and mass of the active material, in accordance with the established relation [52]. At a scan rate of 10 mV s^{-1}, the CeHCF/NPCQD hybrid demonstrates a specific capacitance of 703 F g^{-1}, markedly surpassing that of pristine CeHCF (512 F g^{-1}). This improvement results from the synergistic interplay between the redox-active CeHCF framework and the conductive, defect-rich NPCQDs, which collectively raise the electroactive surface area and accelerate electron transport. As the scan rate increases from 10 to 100 mV s^{-1}, both electrodes exhibit an expected reduction in capacitance due to ion-diffusion constraints at elevated sweep velocities (Fig. 8d). However, the hybrid regularly surpasses the unaltered material, sustaining elevated capacitance values of 648, 604, 559, 525, and 522 F g^{-1} at 20, 30, 50, 80, and 100 mV s^{-1}, respectively. CeHCF provides 471,

437, 392, 348, and 296 F g^{-1} at the respective scan rates. The CeHCF/NPCQD electrode maintains 74.2% of its original capacitance at 100 mV s^{-1}, while CeHCF retains merely 57.8% (Fig. 8e); Table 2). The hybrid's improved rate retention demonstrates its exceptional charge-transfer efficiency, swift ion diffusion, and stable pseudocapacitive response, highlighting its appropriateness for high-rate energy storage applications [53].

GCD Analysis

The galvanostatic charge–discharge properties of the CeHCF and CeHCF/NPCQD electrodes were subsequently assessed at varying current densities of 1–20 A g^{-1}. As shown in Fig. 9a, pristine CeHCF exhibits extended discharge durations and noticeable curvature in the GCD profiles, affirming its faradaic pseudocapacitive behaviour; nonetheless, the slope distortion and considerable iR drop suggest diminished charge-transfer kinetics. Conversely, the CeHCF/NPCQD hybrid electrode demonstrates the longest discharge durations and the most symmetrical charge–discharge patterns, signifying rapid redox kinetics, little internal resistance, and effective charge utilization. The rate capability of the electrodes was examined over a current density range of 1–20 A g^{-1} (Fig. 9c). At 1 A g^{-1}, the CeHCF/NPCQD hybrid delivers a high specific capacitance of 786 F g^{-1}, which is significantly higher than that of pristine CeHCF (583 F g^{-1}) and NPCQDs (64 F g^{-1}). As the current density increases, the hybrid electrode maintains superior performance, retaining 740, 693, 641, 589, and

Table 2 Electrochemical parameters of CeHCF and CeHCF/NPCQD in a three-electrode system

Scan rate (mV s^{-1})	Specific capacitance from CV		Current density (A g^{-1})	Specific Capacitance from GCD	
	CeHCF	CeHCF/NPCQD		CeHCF	CeHCF/NPCQD
10	512 F g^{-1}	703 F g^{-1}	1	583 F g^{-1}	786 F g^{-1}
20	471 F g^{-1}	648 F g^{-1}	3	521 F g^{-1}	740 F g^{-1}
30	437 F g^{-1}	604 F g^{-1}	5	479 F g^{-1}	693 F g^{-1}
50	392 F g^{-1}	559 F g^{-1}	8	433 F g^{-1}	641 F g^{-1}
80	348 F g^{-1}	535 F g^{-1}	10	398 F g^{-1}	589 F g^{-1}
100	296 F g^{-1}	522 F g^{-1}	20	343 F g^{-1}	541 F g^{-1}

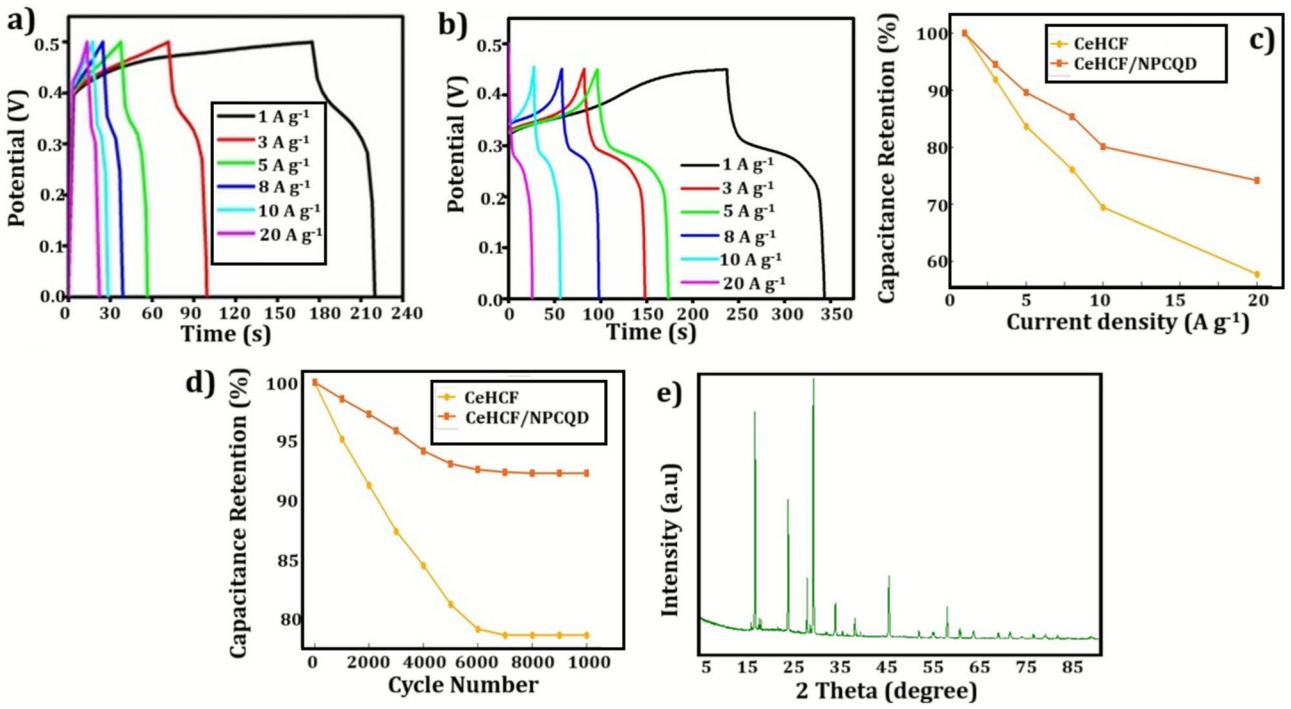

Fig. 9 GCD curves of **(a)** CeHCF **(b)** CeHCF/NPCQD hybrid electrode at different current densities of 1–20 A g^{-1}. **(c)** Comparison of specific capacitance values of CeHCF and CeHCF/NPCQD electrodes as a function of current density **(d)** Cycling stability of CeHCF and CeHCF/NPCQD electrodes over 10,000 charge–discharge cycles at 10 A g^{-1} **(e)** Post cycle XRD pattern of CeHCF/NPCQD

541 F g^{-1} at 3, 5, 8, 10, and 20 A g^{-1}, respectively. In comparison, CeHCF exhibits lower capacitance values of 521, 479, 433, 398, and 343 F g^{-1} at the same current densities. Overall, the CeHCF/NPCQD hybrid retains 68.8% of its capacitance when the current density increases 20-fold from 1 to 20 A g^{-1}, whereas pristine CeHCF retains only 58.8%. The hybrid electrode also demonstrates an excellent coulombic efficiency of ~ 98%, confirming highly reversible charge–discharge behavior with minimal resistive or structural losses. The superior rate performance of CeHCF/NPCQD reflects the combined benefits of its highly conductive, defect-rich NPCQD network and hierarchically accessible mesoporous structure, which collectively facilitate rapid electron transport and efficient electrolyte ion diffusion during high-rate cycling. On the other hand, CeHCF retained only 58.8% under similar conditions, emphasizing the benefit of NPCQD integration for rapid charge transport and better utilization of redox-active sites under high-rate conditions. The charge/discharge times were also used to calculate the coulombic efficiency of both electrodes, which was consistently high (> 96%) across the current range. This indicates that the redox processes are highly reversible and that there is minimal energy loss. The stability of the redox-active interface and the enhanced conductivity provided by the heteroatom-doped carbon quantum dots were particularly evident in the CeHCF/NPCQD electrode, which attained approximately 98.2% coulombic efficiency at 1 A g^{-1}. The CeHCF/NPCQD electrode's long-term cycling stability was assessed in the three-electrode configuration, as illustrated in Fig. 9d. The electrode maintained a coulombic efficiency superior to 95% and retained 92.3% of its initial specific capacitance after 10,000 continuous charge–discharge cycles at a current density of 10 A g^{-1}. This suggests that the redox processes were highly reversible and that there were minimal parasitic side reactions during extended cycling. In order to further verify the hybrid electrode's structural stability after extended cycling, post-cycling XRD analysis was conducted on the CeHCF/NPCQD electrode after 10,000 cycles. The resulting pattern is illustrated in Fig. 9e. The characteristic diffraction peaks of CeHCF are largely preserved, with only a modest reduction in peak intensity. This reduction may be attributed to minor surface relaxation during repeated redox transitions. It is crucial to note that no secondary impurity phases or structural collapse were observed. This confirms that the NPCQD network offers a structural buffering matrix that is effective in preventing lattice distortion or dissolution of the CeHCF framework and in maintaining the integrity of its coordination environment during protracted charge–discharge cycling [54]. The stable CV shape, minimal iR-drop evolution, and low charge-transfer resistance observed in EIS measurements are all consistent with the retention of crystallographic features, which collectively demonstrate the high structural durability of the CeHCF/NPCQD electrode.

EIS Analysis

The interfacial charge transport and ion diffusion behavior of the NPCQD, CeHCF and CeHCF/NPCQD electrodes in a three-electrode configuration were further investigated using electrochemical impedance spectroscopy. The measurements were conducted in 1 M KOH with perturbation amplitude of 5 mV and a frequency range of 100 kHz to 0.01 Hz. Figure 10a presents Nyquist plots for NPCQDs, CeHCF, and the CeHCF/NPCQD hybrid to facilitate a direct comparison of the interfacial charge transport properties of all electrodes. The equivalent series resistance (Rs) was determined from the intercept on the real axis, whereas the charge-transfer resistance (R_{ct}) was calculated from the semicircle diameter in the high-frequency domain. The NPCQD electrode demonstrated a series resistance (Rs) of 2.74 Ω and a comparatively elevated charge transfer resistance (R_{ct}) of 18.62 Ω, indicating its primarily capacitive characteristics with constrained intrinsic redox activity. The pristine CeHCF exhibited a Rs of 2.39 Ω and a R_{ct} of 12.57 Ω, signifying

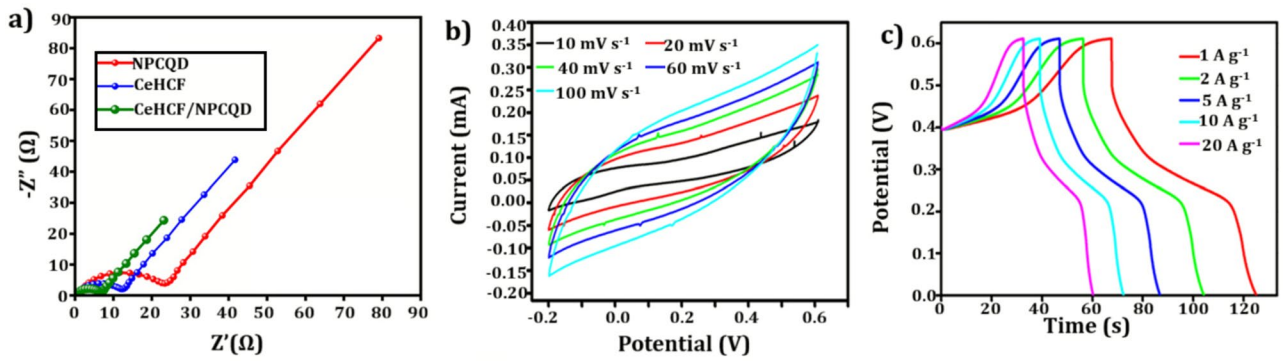

Fig. 10 **(a)** Nyquist plot of NPCQDs, CeHCF and CeHCF/NPCQD **(b)** CV profile of NPCQD at different scan rates (10 mV s^{-1}) **(c)** GCD profile of NPCQD at different current density (1 A g^{-1}- 10 A g^{-1})

enhanced redox activity but limited electron transport owing to its reduced conductivity and dense shape. Conversely, the CeHCF/NPCQD hybrid electrode exhibited a significantly reduced Rs of 1.62 Ω and R_{ct} of 3.84 Ω, substantiating the contribution of NPCQDs in improving electrical connectivity, ion accessibility, and charge-transfer dynamics [55]. The pronounced slope in the low-frequency domain indicates less diffusion resistance and accelerated ion transport within the hybrid structure. Alongside the CV and GCD results, these findings confirm that the CeHCF/NPCQD composite attains a superior equilibrium between pseudocapacitance and conductivity compared to its constituent components. The diminished charge-transfer resistance (R_{ct}) and improved high-rate performance of the CeHCF/NPCQD hybrid can be directly ascribed to the synergistic function of the NPCQDs within the composite. The heteroatom (N, P)-doped carbon domains establish a continuous conductive network on the CeHCF surface, facilitating electron transport and reducing interfacial resistance; nevertheless, their impact extends beyond mere conductivity augmentation. The diminutive dimensions and defect-laden architecture of NPCQDs create interfacial nanochannels and mesoporosity among CeHCF crystallites, facilitating enhanced electrolyte infiltration and superior ion accessibility to interior redox-active regions [56]. This phenomenon is corroborated by the pronounced low-frequency slope in the Nyquist plot, signifying accelerated ion transport and enhanced capacitive charge storage characteristics. The hydrophilic functional groups produced by nitrogen and phosphorus doping enhance electrolyte wettability, ensuring consistent ionic flux across the electrode. Consequently, the NPCQDs serve dual roles as electron-transport facilitators and ion-diffusion enhancers, leading to decreased Rct, improved reversibility of redox processes, and superior rate capability (68.8% capacitance retention at 20 A g^{-1}).

Comparative Electrochemical Performance of NPCQDs, CeHCF, and CeHCF/NPCQD

To further ascertain the synergistic effect of NPCQDs in the hybrid system, the electrochemical performance of NPCQDs alone was evaluated under the same three-electrode conditions (1 M KOH), with the corresponding CV and GCD responses illustrated in Fig. 10b and Fig. 10c, respectively. The NPCQD electrode exhibits a nearly rectangular cyclic voltammetry curve and a reduced discharge duration, resulting in a specific capacitance of approximately 64 F g^{-1} at 1 A g^{-1}, indicating that its charge storage primarily arises from electric double-layer mechanisms, with a minimal pseudocapacitive contribution from surface defects induced by heteroatoms. Conversely, unaltered CeHCF demonstrates an elevated specific capacitance of 583 F g^{-1} at 1 A g^{-1}, resulting from the reversible Ce^{3+}/Ce^{4+} and Fe^{2+}/Fe^{3+} redox reactions. The CeHCF/NPCQD hybrid electrode attains a significantly improved capacitance of 786 F g^{-1} at 1 A g^{-1}, surpassing the capabilities of the separate components considerably. Considering the mass ratio of CeHCF to NPCQDs (about 90:10), the theoretical additive capacitance of the composite, presuming no interaction between the components, may be calculated as:

$$C_{\text{theoretical}} = \left(w_{CeHCF} \times C_{CeHCF}\right) + \left(w_{NPCQD} \times C_{NPCQD}\right)$$

The calculated value is approximately 525 F g^{-1}. The experimentally measured capacitance of 786 F g^{-1} is about 1.5 times greater than the estimated value, clearly indicating a non-linear synergistic enhancement rather than a mere physical mixing effect. This enhancement is ascribed to the conductive and defect-laden NPCQD network, which promotes expedited electron transport, enhanced wettability, and increased accessibility of CeHCF redox-active sites, coupled with a mesoporous interconnected structure that accelerates ion diffusion. The significantly enhanced electrochemical performance of the CeHCF/NPCQD hybrid results from robust interfacial coupling and synergistic electrochemical behavior, validating the effective functional integration of CeHCF and biomass-derived NPCQDs in the composite electrode.

Electrochemical Performance of CeHCF/NPCQD in Two Electrode System

The promising electrochemical behaviour observed in the three-electrode configuration encouraged us to evaluate the CeHCF/NPCQD hybrid under more practical device-level conditions. While three-electrode tests provide fundamental insights into intrinsic capacitance and charge-transfer kinetics, the true applicability of the material must be validated in a two-electrode ASC. Therefore, an ASC was assembled using CeHCF/NPCQD as the positive electrode and activated carbon as the negative electrode to examine whether the high capacitance, rate capability, and stability observed at the electrode scale can be effectively translated into a realistic device configuration. The electrodes were positioned with a Whatman filter paper saturated in electrolyte between them and arranged in a sandwich form under moderate pressure. The schematic (Fig. 11a) distinctly depicts the comprehensive device architecture, highlighting the active material layers, electrolyte-saturated separator, current collectors, and the external circuit connection. For the asymmetric supercapacitor, cyclic voltammetry was initially conducted at 10 mV/s at a variety of potentials (0–1.2 V, 0–1.4 V, 0–1.6 V and 0–1.8 V) in order to identify the safe and effective potential window. As shown in Fig. 11b, the device may be safely operated up to 1.6 V without electrolyte dissolution, according to the steady CV profile in the 0–1.6 V region that

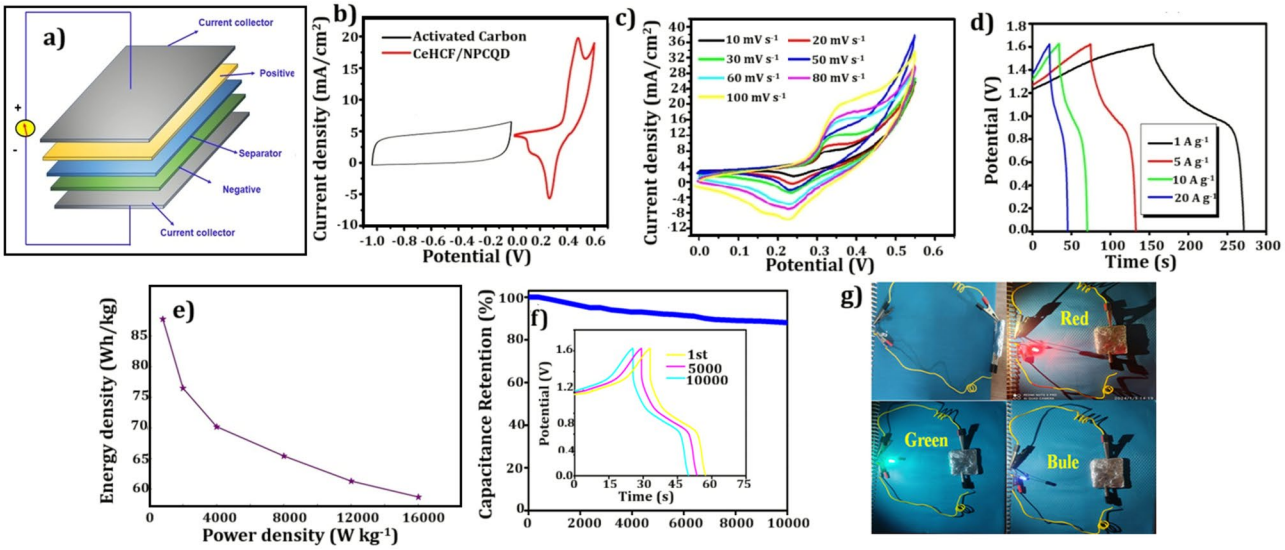

Fig. 11 **(a)** Schematic of the CeHCF/NPCQD//AC asymmetric supercapacitor **(b)** CV curves at various voltage windows; **(c)** CV curves at different scan rates **(d)** GCD curves at various current densities **(e)** Ragone plot **(f)** Cycling performance over 10,000 cycles; **(g)** LED illumination demonstration indicating practical applicability

showed no discernible distortion or polarisation. Therefore, the ideal operating voltage for further CV and GCD measurements in the two-electrode setup was determined to be 1.6 V. The potential window of the ASC device was optimized using CV measurements in the ranges of 0–1.2 V, 0–1.4 V, 0–1.6 V, and 0–1.8 V to ensure the electrochemical stability of the chosen working voltage. The device maintained consistent quasi-rectangular cyclic voltammetry characteristics without any sudden current surge up to 1.6 V, signifying minimal oxygen or hydrogen evolution within this range. The stability at 1.6 V is ascribed to the charge-balance situation between the CeHCF/NPCQD positive electrode and the AC negative electrode, which confines the individual electrode potentials within their non-gas-evolving stability windows. Moreover, during prolonged cycling at 1.6 V, the device exhibited over 95% coulombic efficiency and 91.6% capacitance retention throughout 10,000 cycles, without any distortion in the GCD profile or rise in iR-drop. These observations validate that 1.6 V constitutes a stable and viable operational range for the CeHCF/NPCQD//AC system in aqueous KOH electrolyte, devoid of substantial OER or HER involvement. Moreover, the device's charge storage properties and rate capabilities were examined by recording CV curves at different scan speeds between 10 and 100 mV s^{-1} within the optimised potential range of 0–1.6 V. Figure 11c displays the obtained profiles. Indicating the coexistence of electrical double-layer capacitance from the AC electrode and pseudocapacitive redox reactions from the CeHCF/NPCQD composite, the CV curves have a quasi-rectangular shape with minor redox humps. The hybrid system showed excellent reversibility and rapid electron/ion transport. This was confirmed by the retention of the CV shape at higher scan rates. The overall current response increased proportionally, indicating fast kinetics and good capacitive behaviour. The redox peaks were still visible, although they were slightly shifted. This shift was due to internal resistance and polarisation. The improved performance is mainly due to the synergistic interaction of the pseudocapacitive CeHCF component and the highly conductive nitrogen and phosphorus co-doped carbon quantum dots (NPCQDs). The NPCQDs have many imperfections in their surfaces and electron-rich spots, which improve charge transfer, wettability, and electrochemical utilisation. The CeHCF/NPCQD//AC device's GCD curves were recorded between 0 and 1.6 V, with current densities varying from 1 to 20 A g^{-1} (Fig. 11d). The hybrid capacitive nature including both electric double-layer and pseudocapacitive contributions is confirmed by the almost symmetric charge–discharge patterns with modest non-linearity. The device demonstrated exceptional rate capabilities by delivering a high specific capacitance of 248 F g^{-1} at 1 A g^{-1} and maintaining 66.5% (165 F g^{-1}) even at 20 A g^{-1}. The specific capacitance of the CeHCF/NPCQD//AC device (248 F g^{-1} at 1 A g^{-1}) was determined from the GCD curves using the complete mass of active materials in both electrodes, not only the mass of the positive electrode, to ensure clarity. Since the ASC device incorporates extra elements like internal series resistance, potential distribution across both electrodes and the separator, and charge balance constraints between the positive and negative electrodes, the lower capacitance value seen in the two-electrode system as opposed to the three-electrode configuration (786 F g^{-1} at

1 A g^{-1}) is to be expected. These have an impact on the discharge duration and effective voltage window, which lowers the device-measured capacitance in comparison to the intrinsic capacitance found in the three-electrode configuration. Moreover, the CeHCF/NPCQD electrode's mass loading in the present configuration is maintained at approximately 1.3 mg cm^{-2} to ensure accurate evaluation of the intrinsic electrochemical behavior and uniform wetting. Although this loading is appropriate for laboratory-scale testing, we recognize that commercial-scale supercapacitor devices frequently necessitate a higher mass loading. However, the full utilization of the active material may be impeded by diffusion limitations, non-uniform electrolyte penetration, and increased internal resistance, which may be introduced by increasing electrode thickness. The CeHCF/NPCQD hybrid's hierarchical architecture, which involves the formation of a conductive and ion-accessible network along the CeHCF surface by ultrafine NPCQDs, is advantageous for the mitigation of such effects. This is due to the fact that it promotes accessible porosity and continuous charge-transport pathways. Future research will concentrate on the translation of this architecture into thicker electrodes through the use of scalable processes, such as roll-to-roll lamination or slurry-coating, while maintaining the interconnected pore framework that is crucial for the efficient delivery of ions. The high reversibility and little energy loss are shown by the coulombic efficiency, which stayed over 96%. The synergistic interaction of conductive NPCQDs and redox-active CeHCF, which facilitates quick charge transfer and ion diffusion, is responsible for this improved performance. The practical viability of the fabricated asymmetric supercapacitor is clearly demonstrated by the Ragone plot of the CeHCF/NPCQD//AC device (Fig. 11e), which illustrates the relationship between energy density and power density. The energy and power values were calculated from GCD data using standard equations, incorporating into account the specific capacitance and discharge duration within the optimised voltage window of 1.6 V. The device achieved an impressive energy density of 87.8 Wh kg^{-1} at a power density of 800 W kg^{-1}, surpassing numerous reported Prussian blue analogue-based supercapacitors. The device maintained a substantial energy density of 58.7 Wh kg^{-1}, even at a higher power density of 16,000 W kg^{-1}, which suggests that it can withstand rapid charge–discharge conditions. The synergistic contribution of redox-active cerium hexacyanoferrate and the conductive, heteroatom-rich carbon quantum dots, as well as the expanded voltage window provided by the asymmetric configuration, are responsible for this exceptional energy–power balance. In conclusion, the Ragone plot serves as confirmation of the CeHCF/NPCQD//AC device's exceptional potential for high-energy and high-power supercapacitor applications. The enduring electrochemical stability of the CeHCF/NPCQD//AC device was evaluated by continuous charge–discharge cycling for 10,000 cycles at a current density of 10 A g^{-1}. Figure 11f illustrates that the device maintained 91.6% of its initial specific capacitance after 10,000 cycles, exhibiting just a little decline in performance, hence indicating exceptional longevity and structural integrity. The elevated retention is ascribed to the consistent redox characteristics of cerium hexacyanoferrate and the buffering influence of nitrogen and phosphorus co-doped carbon quantum dots, which facilitate volume adjustments during cycling and reduce electrode deterioration. Moreover, the coulombic efficiency constantly above 95% during the cycling test, indicating highly reversible charge–discharge cycles and minimal energy loss. The results underscore the mechanical integrity and electrochemical durability of the hybrid system, positioning it as a viable option for long-term, practical energy storage applications. Using the fully charged device to power a commercial light-emitting diode (LED) was a straightforward demonstration to evaluate the manufactured CeHCF/NPCQD//AC asymmetric supercapacitor's practicality. As seen in Fig. 11 g, the device was able to successfully light up a red LED (~ 1.8 V operational voltage) for a number of min after being charged to 1.6 V. The potential of the built device to power small-scale electronic devices is demonstrated by this experiment, which amply demonstrates its capacity to store and distribute useable electrical energy. The CeHCF/NPCQD-based hybrid supercapacitor's outstanding energy delivery, quick reaction, and stability are further confirmed by the successful LED lighting, demonstrating its potential for adaptable and portable energy storage applications.

Mechanism for Enhanced Super capacitive Performance

The CeHCF/NPCQD//AC device's superior performance is maintained by a synergistic mechanism that encompasses both faradaic redox reactions and improved charge transport pathways. The primary redox-active material is the CeHCF component, which contributes to pseudo capacitance through reversible Ce^{3+}/Ce^{4+} and Fe^{2+}/Fe^{3+} transitions, as confirmed by XPS analysis. However, the incorporation of nitrogen and phosphorus co-doped carbon quantum dots effectively overcomes the inherently low conductivity of the material. The amorphous nature and ultra-small size of NPCQDs, as confirmed by TEM, promote intimate interfacial contact with the CeHCF crystallites (HRTEM), forming a continuous conductive network that enables rapid electron transport. The XPS spectra of NPCQDs indicate the presence of pyridinic-N, pyrrolic-N, and P–O/P–C functionalities. These functionalities introduce active defect sites and improve electronic conductivity, resulting in enhanced surface redox reactions. Furthermore, BET analysis indicates that the hybrid exhibits a substantial increase in

mesoporosity and surface area (86.7 m^2/g, 2–3.5 nm), which facilitates the rapid diffusion of ions and the accessibility of electrolytes. This mechanism is further supported by electrochemical results: a high b-value of 0.93, a 76% capacitive contribution, and a lower charge transfer resistance (3.84 Ω) observed in EIS corroborate rapid kinetics and surface-controlled charge storage. By integrating redox activity, structural integrity, and conductive pathways in a unified architecture, these features promise that the CeHCF/NPCQD hybrid electrode maintains exceptional capacitance, high-rate capability, and resilient cycling stability.

Comparison with Previous Literature

The CeHCF/NPCQD hybrid's performance was compared with the results of recently reported PBA–carbon composites and rare-earth-based hybrid electrodes in order to assess its practical application (Table 3) [18, 57–68]. A specific capacitance of 248 F g^{-1} at 1 A g^{-1} and a high energy density of 87.8 Wh kg^{-1} at 800 W kg^{-1} were attained in the asymmetric CeHCF/NPCQD//AC device. These values are significantly higher than the average values (< 60 Wh kg^{-1}) reported for the majority of PBA-based ASC systems. The energy-power characteristics that are produced also outperform those of rare-earth systems like Nd_2O_3/PPY (119 F g^{-1} and energy density of 48.5 Wh kg^{-1}) [63], CeO_2@activated carbon (162 F g^{-1} and energy density of 39.2 Wh kg^{-1}) [64], and $LaCoO_3$/rGO (317 F g^{-1} and energy density of 52.2 Wh kg^{-1}) [65]. Additionally, after 10,000 cycles, the device retains 91.6% of its capacity and 66.5% of its capacitance at 20 A g^{-1}, demonstrating its exceptional rate endurance and long-term structural stability. Under similar GCD conditions, the CeHCF/NPCQD electrode outperforms pristine CeHCF (583 F g^{-1}) and surpasses the typical 200–600 F g^{-1} range of Ce-based electrodes reported earlier [66–68]. In the three-electrode configuration, the CeHCF/NPCQD electrode yields 786 F g^{-1} at 1 A g^{-1}. The CeHCF framework's dual Ce^{3+}/Ce^{4+} and Fe^{2+}/Fe^{3+} redox activity, (ii) the conductive, defect-rich NPCQD domains that boost electron delocalization, and (iii) the linked mesoporous network that facilitates quick ion transport and electrolyte wetting are the sources of this improvement. The CeHCF/NPCQD hybrid also showed exceptional cycling stability with 91.6% retention after 10,000 cycles, exceeding the usual stability range of 83–86% of reported PBA and rare-earth oxide systems under comparable testing conditions, and excellent rate capability, maintaining 66.5% of its capacitance at 20 A g^{-1}. The CeHCF/NPCQD electrode demonstrated a specific capacitance of 786 F g^{-1} at 1 A g^{-1}, which was significantly higher than pristine CeHCF (583 F g^{-1}), confirming the enhanced electrochemical utilization made possible by NPCQD incorporation. All things considered, the CeHCF/NPCQD hybrid successfully combines redox-active coordination frameworks with a biomass-derived, sustainable carbon architecture, striking a strong balance between high capacitance, high energy density, quick charge–discharge kinetics, and exceptional cycling stability. These characteristics make the CeHCF/NPCQD electrode a promising option for scalable supercapacitor systems of the future.

Conclusions

In summary, a novel hybrid supercapacitor electrode based on CeHCF and NPCQD was successfully synthesized and evaluated. Structural and morphological characterizations confirmed the formation of a well-integrated composite with enhanced surface area, mesoporosity and strong interfacial

Table 3 Comparison of electrochemical performance parameters of CeHCF/NPCQD with previously reported PBA-based hybrid electrode materials in asymmetric configurations

Electrode material	Specific capacitance (F g^{-1})	Energy density (Wh Kg^{-1})	Capacitance retention (%)	References
NiHCF/CNF	507 F g^{-1}	60 Wh kg^{-1}	67% 5000 cycles	[57]
CoHCF/C dot	394 F g^{-1}	48.6 Wh kg^{-1}	88% in 5000 cycles	[58]
FeCoHCF	560 F g^{-1}	40 Wh kg^{-1}	90% 10,000 cycles	[59]
CoHCF/MnO_2	385 F g^{-1}	37.6 Wh kg^{-1}	86% in 5000 cycles	[60]
C dot/PBA/Ni foam	659 F g^{-1}	65 Wh kg^{-1}	91% in 1000 cycles	[61]
CoHCF/PPY/CNT	495 F g^{-1}	38.6 Wh kg^{-1}	80% in 4500 cycles	[62]
MnHCF/PANI/C	730 F g^{-1}	56.5 Wh kg^{-1}	85% in 1000 cycles	[18]
Nd_2O_3/Polypyrrole	119 F g^{-1}	48.5 Wh kg^{-1}	88% in 3000 cycles	[63]
CeO_2/Activated C	162 F g^{-1}	39.2 Wh kg^{-1}	90 & in 2000 cycles	[64]
$LaCoO_3$/rGO	317 F g^{-1}	52.2 Wh kg^{-1}	76% in 5000 cycles	[65]
CeO_2	400 F g^{-1}	20 Wh kg^{-1}	82% in 10,000 cycles	[66]
Ce/NiO	110 F g^{-1}	26.2 Wh kg^{-1}	91.6% in 1000 cycles	[67]
CeO_2	134 F g^{-1}	41.5 Wh kg^{-1}	92.5% in 1000 cycles	[68]
CeHCF/NPCQD	786 F g^{-1}	87.8 Wh kg^{-1}	91.6% in 10,000 cycles	This work

contact between the components. The CeHCF/NPCQD electrode exhibited superior electrochemical performance in both three- and two-electrode systems. In the two-electrode asymmetric device (CeHCF/NPCQD//AC), a high specific capacitance of 248 F g^{-1} at 1 A g^{-1}, energy density of 87.8 Wh kg^{-1}, and outstanding cycling stability of 91.6% retention after 10,000 cycles were achieved. The exceptional performance is attributed to the synergistic redox behavior of Ce and Fe centers, combined with the enhanced conductivity, defect-rich surface, and ion-accessible porous network provided by NPCQDs. Beyond performance, the synthesis relies on low-cost, widely available precursors and eco-friendly aqueous processing, making it scalable for bulk production. By integrating waste valorization with green synthesis, the approach minimizes life-cycle environmental impact while delivering cost-effective and durable energy storage. Overall, the close agreement between the high intrinsic capacitance observed in the three-electrode tests and the excellent performance of the assembled asymmetric device confirms that the CeHCF/NPCQD hybrid can reliably translate electrode-level advantages into practical device-level outcomes, reinforcing its potential for real-world supercapacitor applications.

Author Contribution D. Sivaguru Nathan, performed conceptualization, experimental design, methodology, formal analysis and writing—original draft. Dr. S. Kumaran performed review and editing. Dr. K. Umapathy contributed to software and validation. Dr. Simon Deepa contributed to data interpretation. Dr. R. A. Kalaivani coordinating the research activity, including planning and data supervision, project administration and funding acquisition. Dr. P. Siva Karthik contributed to literature review, manuscript formatting and proofreading. All authors reviewed the results and approved the final version of the manuscript.

Funding No funding obtained for this study.

Data Availability All data analyzed during the study are included in this article and will be made upon reasonable request.

Declarations

Conflicts of interest The author(s) declare that there is no conflict of interest regarding the publication of this article.

References

1. Xue, C., Shahbaz, M., Ahmed, Z., Ahmad, M., Sinha, A.: Clean energy consumption, economic growth, and environmental sustainability: what is the role of economic policy uncertainty? Renew. Energy **184**, 899–907 (2022)
2. Singh, S.: Energy crisis and climate change: Global concerns and their solutions. *Energy: crises, chall solut.* 1–17. (2021)
3. Jin, J., Geng, X., Chen, Q., Ren, T.L.: A better Zn-ion storage device: recent progress for Zn-ion hybrid supercapacitors. Nano-Micro Lett. **14**(1), 64 (2022)
4. Parveen, N., Da'na, E., Taha, A.: Sustainable fabrication of Fe_2O_3/C nanoparticles via *Acacia nilotica* extract for enhanced supercapacitor performance. Nanotechnology **36**(11), 115704 (2025)
5. Ren, K., Liu, Z., Wei, T., Fan, Z.: Recent developments of transition metal compounds-carbon hybrid electrodes for high energy/power supercapacitors. Nano-Micro Lett. **13**(1), 129 (2021)
6. Hussain, S., Vikraman, D., Mehran, M.T., Hussain, M., Nazir, G., Patil, S.A., Jung, J.: Ultrasonically derived WSe2 nanostructure embedded MXene hybrid composites for supercapacitors and hydrogen evolution reactions. Renew Energy. **185**, 585–597 (2022)
7. Shaikh, J.S., Shaikh, N.S., Sabale, S., Parveen, N., Patil, S.P., Mishra, Y.K., Kanjanaboos, P., Praserthdam, S., Lokhande, C.D.: A phosphorus integrated strategy for supercapacitor: 2D black phosphorus–doped and phosphorus-doped materials. Mater. Today Chem. **21**, 100480 (2021)
8. Kumar, A., Rathore, H.K., Sarkar, D., Shukla, A.: Nanoarchitectured transition metal oxides and their composites for supercapacitors. Electrochem. Sci. Adv. **2**(6), e2100187 (2022)
9. Al-Abawi, B.T., Parveen, N., Ansari, S.A., Al-Dosari, H.A., Alshaikh, H.K., Umar, A., Akbar, S.: Emerging trends in nickel sulfide electrodes for high-performance supercapacitors: synthesis, mechanisms, and nanocomposite innovations. Int J Energy Res **2025**(1), 5331742 (2025)
10. Parveen, N.: Enhanced energy storage using bio-waste derived carbon and three-dimensional $NiCo_2O_4$ structures in asymmetric supercapacitors. J. Ind. Eng. Chem. (2025). https://doi.org/10.1016/j.jiec.2025.06.027
11. Dayanithy, M., Sekhar, G.C., Thivyarathi, R.C., Divyabharathi, P., Maguluri, L.P., Saravanan, V.: Synergistic integration of $NiCo_2O_4$ and $NiWO_4$ nanosheets on Ni foam for advanced supercapacitor applications. J. Porous Mater. (2025). https://doi.org/10.1007/s10934-025-01829-3
12. Saravanan, V., Arthy, M., Jayakar, S.A., Suganya, S., Archana, T., Thirumalai, M.: Hierarchical $ZnCo_2O_4$/MoS_2@ rGO nanocomposite on nickel foam: a promising electrode for advanced energy storage. Ionics (2025). https://doi.org/10.1007/s11581-025-06399-7
13. Fu, X., Ren, L., Tian, H., Sun, Z., Jin, Y., Wang, D., Yang, H.: Facile synthesis of cryogenically controlled cobalt-nickel-based Prussian blue analogues for high-performance symmetric supercapacitors. J Alloys Compd. **992**, 174606 (2024)
14. Ma, G., Zhou, X., Cao, Y., Guan, X., Wu, W., Zhang, S., Li, C., Kong, Z., Wang, S.: Sulfonated polyaniline coated Prussian blue analog derived Mn-Fe oxide composite electrode for all-solid-state flexible supercapacitors. Chem. Eng. J. **508**, 160942 (2025)
15. Yang, Y., Hao, Y., Niu, L., Xia, F.: In situ co-deposition of nickel hexacyanoferrate nanocubes on the reduced graphene oxides for supercapacitors. Carbon **84**, 174–184 (2015)
16. Pires, B.M., Nunes, W.G., Freitas, B.G., Oliveira, F.E.R., Katic, V., Rodella, C.B., Zanin, H.: Characterization of porous cobalt hexacyanoferrate and activated carbon electrodes under dynamic polarization conditions in a sodium-ion pseudocapacitor. J. Energy Chem. **54**, 53–62 (2021)
17. Meng, F., Tu, X., Liu, Y., Wang, K., Xu, X., Liu, X., Pan, L.: Carbon nanotube sustained ternary-metal Prussian blue analogues for superior-performance rocking-chair capacitive deionization. Sep. Purif. Technol. **329**, 125155 (2024)
18. Babu, R.S., de Barros, A.L.F., de Almeida Maier, M., da Motta Sampaio, D., Balamurugan, J., Lee, J.H.: Novel polyaniline/manganese hexacyanoferrate nanoparticles on carbon fiber as binder-free electrode for flexible supercapacitors. Compos. Part B Eng. **143**, 141–147 (2018)
19. Peng, J., Li, C., Yin, J., Wang, J., Yu, Y., Shen, Y., Huang, Y.: Novel cerium hexacyanoferrate (II) as cathode material for

sodium-ion batteries. ACS Appl. Energy Mater. **2**(1), 187–191 (2018)
20. Yang, H., Lu, B., Guo, L., Qi, B.: Cerium hexacyanoferrate/ordered mesoporous carbon electrode and its application in electrochemical determination of hydrous hydrazine. J. Electroanal. Chem. **650**(2), 171–175 (2011)
21. Ansari, S. A., Parveen, N., Ansari, M. Z., Alsulaim, G. M., Alam, M. W., Khan, M. Y., & Zhang, K.: Exploring recent advances in the versatility and efficiency of carbon materials for next generation supercapacitor applications: a comprehensive review. *Prog Mater Sci*, 101493 (2025)
22. Parveen, N., Ansari, S.A., Alnahdi, K.M., Hammud, H.H., Aljamhi, W.A., Alam, M.W., Al Zoubi, W.: Eco-friendly synthesis and applications of graphene-titanium dioxide nanocomposites for pollutant degradation and energy storage. J. Photochem. Photobiol. A Chem. **459**, 116096 (2025)
23. Zhang, X., Wang, J., Liu, J., Wu, J., Chen, H., Bi, H.: Design and preparation of a ternary composite of graphene oxide/carbon dots/polypyrrole for supercapacitor application: importance and unique role of carbon dots. Carbon **115**, 134–146 (2017)
24. Wang, R., Wang, H., Zhou, Y., Gao, Z., Han, Y., Jiang, K., Wu, D.: Green synthesis of N-doped porous carbon/carbon dot composites as metal-free catalytic electrode materials for iodide-mediated quasi-solid flexible supercapacitors. Inorg. Chem. Front. **9**(11), 2530–2543 (2022)
25. Vinayagam, M., Babu, R.S., Sivasamy, A., de Barros, A.L.F.: Biomass-derived porous activated carbon from *Syzygium cumini* fruit shells and *Chrysopogon zizanioides* roots for high-energy density symmetric supercapacitors. Biomass Bioenergy **143**, 105838 (2020)
26. Abinaya, K., Rajkishore, S.K., Lakshmanan, A., Anandham, R., Dhananchezhiyan, P., Praghadeesh, M.: Synthesis and characterization of carbon dots from coconut shell by optimizing the hydrothermal carbonization process. J Appl Nat Sci (2021). https://doi.org/10.31018/jans.v13i4.2916
27. Zhang, K., Lee, T.H., Cha, J.H., Varma, R.S., Choi, J.W., Jang, H.W., Shokouhimehr, M.: Cerium hexacyanocobaltate: a lanthanide-compliant Prussian blue analogue for Li-ion storage. ACS Omega **4**(25), 21410–21416 (2019)
28. Tadesse, A., Belachew, N., Hagos, M., Basavaiah, K.: Synthesis of fluorescent nitrogen and phosphorous co-doped carbon quantum dots for sensing of iron, cell imaging and antioxidant activities. J. Fluoresc. **31**, 763–774 (2021)
29. Kaplun, M.M., Smirnov, Y.E., Mikli, V., Malev, V.V.: Structure of cobalt hexacyanoferrate films synthesized from a complex electrolyte. Russ. J. Electrochem. **37**, 914–924 (2001)
30. Feng, L.D., Gu, M.M., Yang, Y.L., Liang, G.X., Zhang, J.R., Zhu, J.J.: Electrochemical synthesis for flowerlike and fusiform christmas-tree-like cerium hexacyanoferrate (II). J. Phys. Chem. C **113**(20), 8743–8749 (2009)
31. de Oliveira, D.R., Fernandes, D.S., do Carmo, D.R.: A cerium hexacyanoferrate (III) nanoparticle-modified carbon paste electrode: voltammetric characterization and behavior in the presence of dopamine. Electroanalysis **32**(7), 1524–1532 (2020)
32. Devadas, B., Cheemalapati, S., Chen, S.M., Rajkumar, M.: Investigation of morphologies and characterization of rare earth metal samarium hexacyanoferrate and its composite with surfactant intercalated graphene oxide for sensor applications. RSC Adv. **4**(86), 45895–45902 (2014)
33. Arunprasad, V., Rapur, P., Hemanand, D., Bennet, M.A., Saravanan, V.: Design and fabrication of nanoarchitectures of rGO-decorated ZnCo2O4 hybrid photocatalyst for high-efficiency solar fuel generation. J. Mater. Sci. Mater. Electron. **36**(3), 192 (2025)
34. Manjula, N., Pulikkutty, S., Chen, T.W., Chen, S.M., Liu, X.: Hexagon prism-shaped cerium ferrite embedded on GC electrode for electrochemical detection of antibiotic drug ofloxacin in biological sample. Colloids Surf A Physicochem Eng Asp **627**, 127129 (2021)
35. Zeng, G., Chen, Y., Chen, L., Xiong, P., Wei, M.: Hierarchical cerium oxide derived from metal-organic frameworks for high performance supercapacitor electrodes. Electrochim. Acta **222**, 773–780 (2016)
36. Krishnan, P.H., Sul, R.D., Murugan, M.S., Saravanan, V.: Optimization of La and Ce mixed metal oxide hybrid for enhanced photoresponse in UV–Visible photosensing applications. J. Mater. Sci. Mater. Electron. **36**(22), 1377 (2025)
37. Maran, S., Kumar, M.D.: Facile synthesis of bio-carbon supported cobalt hexacyanoferrate hybrid photocatalyst for effective removal of hazardous organic pollutants. Ionics **30**(12), 8771–8784 (2024)
38. Prabhu chandran, K., Nath, S.S., Sudha, K., Vinod Kumar, T., Kumaran, S., Sasidevi, J.: Strategic design of TiO2-SnS hybrid nanostructures: dual-function catalysts for antibiotic removal and solar energy conversion in DSSCs. J. Electron. Mater. (2025). https://doi.org/10.1007/s11664-025-12377-6
39. Sengeni, D., Nadanasabai, R., Saravanan, V., Sangeetha, L., Prakash, J.U.: Development of binary transition metallic selenide (NiSe/Co3Se4) hybrid counter electrode for highly efficient Pt-free dye-sensitized solar cells. Ionics **30**(12), 8281–8293 (2024)
40. Syamala, M., Srivastava, D., Khandekar, S.D., Porselvi, T., Patan, M.K., Balaram, A., Kumaran, S.: Construction of g-C3N4 anchored Cu-ZnS hybrid nanostructures for sustainable energy storage and environmental remediation. Res. Chem. Intermed. (2025). https://doi.org/10.1007/s11164-025-05713-2
41. Alamdari, N.G., Almasi, H., Moradi, M., Akhgari, M.: Characterization of carbon quantum dots synthesized from vinasse and date seeds as agro-industrial wastes. Waste Biomass Valoriz. **14**(11), 3689–3703 (2023)
42. Ansari, S.A.: Fabrication and evaluation of binder-free metal-molybdate electrodes for improved energy storage and hydrogen evolution applications. J. Power. Sources **646**, 237185 (2025)
43. Nath, S. S., Chanthirasekaran, K., Priya, S. S., Bharathirja, N., Gupta, D., & Kumaran, S.: Boosting electrochemical behavior of biomass-derived porous carbon via N, S, and N, S co-doping for enhanced supercapacitor performance. *Diam Relat Mater*, 112850. (2025)
44. Zhai, X.Z., Qu, J., Wang, J., Chang, W., Liu, H.J., Liu, Y.H., Yu, Z.Z.: Diffusion-driven fabrication of yolk-shell structured K-birnessite@ mesoporous carbon nanospheres with rich oxygen vacancies for high-energy and high-power zinc-ion batteries. Energy Storage Mater. **42**, 753–763 (2021)
45. Ansari, S. A., Alam, M. W., BaQais, A., & Yewale, M. A.: Exploring the effective electrochemical diclofenac sensing, energy storage, and photocatalytic capabilities of strontium-doped molybdenum oxide nanoparticles. *J Ind Eng Chemi*. (2025)
46. Patra, A., Namsheer, K., Jose, J.R., Sahoo, S., Chakraborty, B., Rout, C.S.: Understanding the charge storage mechanism of supercapacitors: in situ/operando spectroscopic approaches and theoretical investigations. J. Mater. Chem. A **9**(46), 25852–25891 (2021)
47. Kumar, N., Kim, S.B., Lee, S.Y., Park, S.J.: Recent advanced supercapacitor: a review of storage mechanisms, electrode materials, modification, and perspectives. Nanomaterials **12**(20), 3708 (2022)
48. Ansari, M.Z., Ansari, S.A., Parveen, N., Alam, M.W., Kim, S.H.: The role of high-entropy materials and d-band center adjustments in supercapacitor development. J. Energy Storage **131**, 117535 (2025)
49. Bhojane, P., Shirage, P.M.: Facile preparation of hexagonal WO3 nanopillars and its reduced graphene oxide nanocomposites for high-performance supercapacitor. J. Energy Storage **55**, 105649 (2022)

50. Kalu-Uka, G.M., Kumar, S., Kalu-Uka, A.C., Vikram, S., Ihekweme, G.O., Ranjan, N., Kumar, S.: Production of activated carbon electrode for energy storage application in supercapacitors via KOH activation of waste termite biomass. Waste Biomass Valoriz. (2022). https://doi.org/10.1007/s12649-022-01680-6
51. Martinez-Casillas, D.C., Mascorro-Gutierrez, I., Betancourt-Mendiola, M.L., Palestino, G., Quiroga-Gonzalez, E., Pascoe-Sussoni, J.E., Cuentas-Gallegos, A.K.: Residue of corncob gasification as electrode of supercapacitors: an experimental and theoretical study. Waste Biomass Valoriz. **12**, 4123–4140 (2021)
52. Wang, X., Yang, S., Shen, B., Yang, J., Xu, L.: Pyrolysis of biomass pineapple residue and banana pseudo-stem: kinetics, mechanism and valorization of bio-char. Catalysts **12**(8), 840 (2022)
53. Kumar, R., Ranjan, B., Kaur, D.: Pseudocapacitive performance of reactively co-sputtered titanium chromium nitride nanopyramids towards flexible supercapacitor with Li-ion storage. J. Energy Storage **84**, 110866 (2024)
54. Rajeshkumar, L., Ramesh, M., Bhuvaneswari, V., Balaji, D.: Carbon nano-materials (CNMs) derived from biomass for energy storage applications: a review. Carbon Lett. **33**(3), 661–690 (2023)
55. Sivakumar, P., Raj, C.J., Savariraj, A.D., Manikandan, R., Karuppasamy, K., Alfantazi, A., Jung, H.: The interwoven structured two-dimensional NiCo layered double hydroxide tortuous nanosheet as performance-enhanced electrode material toward battery-type supercapacitor. Int. J. Energy Res. **2024**(1), 3149906 (2024)
56. Sivakumar, P., Kulandaivel, L., Park, J., Raj, C.J., Manikandan, R., Jung, H.: MOF-derived flower-like ZnCo2O4/ZnO nanoarchitecture as a high-performance battery-type redox-active electrode material for hybrid supercapacitor applications. J. Alloys Compd. **952**, 170042 (2023)
57. Tang, Z., Shang, X., Hu, B., Nie, P., Shi, W., Yang, J., Liu, J.: Fabrication of various metal hexacyanoferrates@ CNF through acid-regulation for high-performance supercapacitor with superior stability. Carbon **187**, 47–55 (2022)
58. Song, Z., Liu, W., Zhou, Q., Du, J., Chen, J., Wei, X., Zhao, Z.: Coordination-induced activation of reversible Co (II)/Co (III) redox reaction in carbon nanodots/cobalt hexacyanoferrate composites with enhanced electrochemical performance. J. Alloys Compd. **893**, 162368 (2022)
59. Mathi, S., Khouqeer, G.A., Ashok, V., Gayathri, A., AbdelAll, N., Alodhayb, A., Shetti, N.P.: Enhanced supercapacitor performance with mixed-valence Fe-Co hexacyanoferrate nanostructures as stable, high-efficiency electrode materials. Electrochim. Acta (2025). https://doi.org/10.1016/j.electacta.2025.146435
60. Song, Z., Liu, W., Zhou, Q., Zhang, L., Zhang, Z., Liu, H., Zhao, Z.: Cobalt hexacyanoferrate/MnO2 nanocomposite for asymmetrical supercapacitors with enhanced electrochemical performance and its charge storage mechanism. J. Power. Sources **465**, 228266 (2020)
61. Guo, Z., Song, R., Zhang, L., Li, Z., Yao, H., Liu, Q., Li, Z.: Three-dimensional carbon dots/Prussian blue analogues nanocubes/nickel foams as self-standing electrodes for high-performance hybrid electrochemical capacitors. J. Colloid Interface Sci. **613**, 796–805 (2022)
62. Baykara, E.A., Zeybek, B.: The preparation of polypyrrole/carboxyl functionalized multi-walled carbon nanotube@ cobalthexacyanoferrate hybrid composite for high-performance supercapacitor application. J. Energy Storage **73**, 109091 (2023)
63. Abdollahi, F., Shahidi-Zandi, M., Foroughi, M.M., Kazemipour, M.: Electrochemical investigation of polypyrrole/Nd2O3 nanocomposite as high performance supercapacitor material on mild steel substrate. Int. J. Electrochem. Sci. **15**(12), 11757–11768 (2020)
64. Aravinda, L.S., Bhat, K.U., Bhat, B.R.: Nano CeO2/activated carbon based composite electrodes for high performance supercapacitor. Mater. Lett. **112**, 158–161 (2013)
65. Vats, A.K., Kumar, A., Rajput, P., Kumar, A.: Engineered perovskite LaCoO3/rGO nanocomposites for asymmetrical electrochemical supercapacitor application. J. Mater. Sci. Mater. Electron. **33**(5), 2590–2606 (2022)
66. Junais, P.M., Athika, M., Govindaraj, G., Elumalai, P.: Supercapattery performances of nanostructured cerium oxide synthesized using polymer soft-template. J. Energy Storage **28**, 101241 (2020)
67. Gawali, S.R., Dubal, D.P., Deonikar, V.G., Patil, S.S., Patil, S.D., Gomez-Romero, P., Pant, J.: Asymmetric supercapacitor based on nanostructured Ce-doped NiO (Ce: NiO) as positive and reduced graphene oxide (rGO) as negative electrode. ChemistrySelect **1**(13), 3471–3478 (2016)
68. Prasanna, K., Santhoshkumar, P., Jo, Y.N., Sivagami, I.N., Kang, S.H., Joe, Y.C., Lee, C.W.: Highly porous CeO2 nanostructures prepared via combustion synthesis for supercapacitor applications. Appl. Surf. Sci. **449**, 454–460 (2018)